

Supplementary Materials for

Well-defined nanostructuring with programmable anodic aluminium oxide template

Rui Xu, Zhiqiang Zeng, Yong Lei*

Correspondence to: yong.lei@tu-ilmenau.de

This PDF file includes:

Methods

Supplementary Figs. 1 to 36

Methods

Atomic layer deposition. Atomic layer deposition (ALD) was performed with a Picosun SUNALETM R150 ALD system. For TiO₂ growth, the ALD deposition was carried out at 300 °C with a growth rate of about 0.05 nm per cycle. A typical growth cycle includes 0.1 sec pulsing of titanium (IV) chlorides, 5 sec purging of nitrogen, 0.1 sec pulsing of deionized (DI) water, and 5 sec purging of nitrogen. For SnO₂ growth, the ALD deposition was carried out at 250 °C with a growth rate of about 0.03 nm per cycle. A typical growth cycle involves 0.5 sec pulsing of tin (IV) chloride, 10 sec purging of nitrogen, 0.5 sec pulsing of DI water, and 10 sec purging of nitrogen. For metallic Pt, the ALD deposition was carried out at 300 °C with a typical growth cycle of 1.5 sec pulsing of Pt(MeCp)Me₃, 30 sec filling of nitrogen, 20 sec purging of nitrogen, 1.5 sec pulsing of oxygen, 30 sec filling of nitrogen, and 20 sec purging of nitrogen.

Electrochemical deposition. Two-electrode configuration was exploited for all electrochemical deposition using an electrochemical workstation (BioLogic). Ni deposition was performed in an aqueous solution (0.12 M NiCl₂, 0.12 M Ni₂SO₄, and 0.5 M H₃BO₃) at a constant current density of 2 mA/cm² with a Ni plate as counter electrode. Au and Ag deposition were conducted at a constant current density of 1 mA/cm² with counter electrode of a Pt foil in the plating solutions.

Material etching. The unanodized aluminium foil was etched in a mixture solution including 3.4 g CuCl₂, 100 ml HCl, and 100 ml DI water at room temperatures. The anodic aluminium oxide (AAO) template was wet-chemically etched in 0.5 M H₃PO₄ solutions or 0.1 M NaOH solutions. For keeping a constant etching rate for AAO template, the wet-chemical etching was always conducted at a constant temperature of 30 °C. Dry etching upon AAO template was performed by an argon ion milling system (Gatan PECSTM) with an etching power of 4.5 kV, rotation frequency of 2 Hz, and tilted angle of 60°.

Fabrication of Ni imprint stamp with clover-like nanopillars. To obtain a Ni stamp with a tetragonal array of four-leaf clover-like nanopillars, a commercially available Si mold patterned with circular nanodents on its surface was exploited, which are of 400 nm spacing and tetragonally arranged. First, the Si mold was cleaned in a mixture solution (H₂O₂:H₂SO₄, 1:3) at 100 °C for 1 hr. After cleaning in DI water, the Si mold was treated using 3-aminopropyltriethoxysilane (3-APTES, 1.0 v% in CH₃CH₂OH) at 60 °C for 1.5 hr. Then, a gold layer (thickness of about 15 – 25 nm) was evaporated onto the nanopatterned surface of the Si mold by physical vapor deposition (PVD) system, serving as a conductive layer in the following electrochemical deposition. Afterwards, a thick Ni layer was electrodeposited at a constant current density of 2 mA/cm². After the electrochemical deposition, the Ni foil was dried by airflow and peeled off from the Si mold. Accordingly, a Ni foil equipped with a tetragonal array of circular nanopillars was obtained.

The as-obtained circular nanopillars were then utilized for patterning an aluminium foil surface by mechanical impressing under a pressure of 10 kN cm⁻² (Supplementary Fig. 4a₁). The imprinted area was then anodized in 0.4 M H₃PO₄ solutions at an anodization voltage (AV) of

160 V at 10 °C for 10 min, leading to a porous AAO template (Supplementary Fig. 4a₂). Afterwards, polymethyl methacrylate (PMMA) was dripped onto the anodized area and dried naturally to form a supporting layer. After wet-chemically removing the unanodized aluminium foil (Supplementary Fig. 4a₃), the exposed AAO template was selectively etched in 0.5 M H₃PO₄ solutions for 90 min, and then covered by a gold layer (thickness of about 15 – 20 nm) by PVD (Supplementary Fig. 4a₄). With this conductive layer as working electrode, Ni electrodeposition was performed to form a thick layer (Supplementary Fig. 4a₅). After dissolving the supporting PMMA layer in dimethyl sulfoxide solution at 80 °C for 2 hr and completely removing the AAO template in the H₃PO₄ solution for 5 hr, a Ni stamp with a tetragonal array of four-leaf clover-like nanopillars was obtained (Supplementary Fig. 4a₆). The as-fabricated nanopillars are shown in Supplementary Fig. 4b,c.

Similarly, we fabricated another Ni imprint stamp with a hexagonal array of three-leaf clover-like nanopillars (Supplementary Fig. 7). The fabrication process (Supplementary Fig. 7a) was nearly the same as that for the Ni stamp with a tetragonal array of four-leaf clover-like nanopillars, except for that it started with a Si mold patterned with a trigonal array of circular nanodents. Finally, a Ni stamp with a hexagonal array of three-leaf clover-like nanopillars was constructed, as shown in Supplementary Fig. 7b,c.

Anodic anodization of aluminium. For predetermining nanodents on aluminium foils to guide pore evolution during anodization, Ni stamps with arrayed nanopillars were exploited for engineering electro-polished aluminium foils by an imprinting system at a constant pressure of 10 kN cm⁻² for 3 min. Aluminium foils patterned with nanodents of hexagonal arrangement and $400/\sqrt{3}$ nm spacing were always anodized in 0.4 M H₃PO₄ solutions regardless of the applied AV. Regarding aluminium foils patterned with nanodents of tetragonal arrangement and 400 nm spacing, the anodization electrolytes were selected on the base of AVs: as for AVs lower than 180 V, anodization was conducted in 0.4 M H₃PO₄ solutions; while beyond 180 V, a mixture solution including 3 mL H₃PO₄, 300 ml ethylene glycol, and 600 ml DI water was exploited that can mitigate electrolytic breakdown of AAO template at high AVs.

Synthesis of nanostructure arrays with AAO templates. To construct Ag nanoparticles with in-plane different shapes (S1 to S5 in Fig. 6a-d), the lab-made Ni stamp with a hexagonal array of three-leaf clover-like nanopillars was exploited to engineer aluminium surface. At different AVs (e.g., 150, 140, 120, 100, and 80 V), the nanodents inheriting the geometrical features of Ni three-leaf clover-like nanopillars were evolved into pores of different shapes during anodization. After anodization, a 50-nm-thick Ag layer was evaporated onto the anodized area by PVD, serving as a conductive layer. Then, Ag electrodeposition was performed to form a thick substrate. After wet-chemically removing the unanodized aluminium foil and the AAO template, arrays of in-plane shape-different Ag nanoparticles were obtained.

For fabricating out-of-plane shape-different Au nanowires (S6 to S10 in Fig. 6e-h), the Ni stamp with tetragonally arranged four-leaf clover-like nanopillars was exploited to pattern aluminium

foils. Upon the imprinted area, sequential anodization was conducted at different AVs to tune the out-of-plane pore shape. Taking Au nanowires combining five shapes (S10) as an example, five-step anodization at 120 V for 20 min → 140 V for 7.5 min → 160 V for 5 min → 180 V for 15 min → 200 V for 10 min was sequentially performed to fabricate five-shape combined pores. Then, a 5-nm-thick TiO₂ layer was deposited along the pore walls by ALD to tune the dielectric environment of the following Au nanowires and meanwhile endow the high-aspect-ratio Au nanowires with mechanical robustness. To form a supporting substrate for Au nanowires, we deposited a metallic layer (5-nm-thick Ti and 20-nm-thick Au) onto the template, serving as working electrode in the following Au and Ni electrodeposition. After completing Au and Ni electrodeposition, the unanodized aluminium foil on the backside was wet-chemically removed, followed by ion-milling off the pore barrier. When the Au plating solution can penetrate through pores and touch the conductive substrate, Au electrodeposition was carried out, and the resultant Au nanowires replicated the structural features of pores. Finally, an array of Au nanowires combining five shapes in the axial direction was obtained after wet-chemically dissolving the AAO template in NaOH solutions. Using the same way, we fabricated pores combining one, two, three, and four shapes as well as the resulting Au nanowire arrays. Taking changeable pore-elongation rates at different AVs into consideration, the anodization parameters for the other four samples were 200 V for 50 min (S6), 180 V for 38 min → 200 V for 25 min (S7), 160 V for 8 min → 180 V for 25 min → 200 V for 17 min (S8), and 140 V for 9 min → 160 V for 6 min → 180 V for 19 min → 200 V for 12.5 min (S9) to maintain the same length for all Au nanowires.

For constructing TiO₂ nanotubes and TiO₂-nanotubes/Au-nanowires combinations (S11 to S15 in Fig. 6i-l), we exploited the Ni stamp with a tetragonal array of four-leaf clover-like nanopillars to engineer aluminium foils. Under the AVs of 140, 160, and 200 V, the 1st-set pores evolved into star, square, and circular shapes, respectively. A 40-nm-thick TiO₂ layer was then grown along the pore walls by ALD to serve as semiconductor photocatalyst. After ion-milling off the TiO₂ layer on the topmost surface, a metallic layer (5-nm-thick Ti and 20-nm-thick Au) was evaporated onto the top surface by PVD, followed by Ni electrodeposition to form a supporting substrate. Afterwards, the unanodized aluminium foil and the AAO template were wet-chemically etched, leading to TiO₂ nanotubes with different shapes (S11 to S13). For obtaining TiO₂-nanotubes/Au-nanowires arrays, the 2nd-set pores were opened at the fourfold junction sites of neighboring 1st-set pores using NaOH solutions for 20 min. The opened 2nd-set pores were then isotropically etched in NaOH solutions to form a circular shape truncated with 4 voids or selectively etched in H₃PO₄ solutions to form an 8-edged cross shape. With the exposed conductive substrate as working electrode, Au electrodeposition was conducted in the 2nd-set pores to form shape-different Au nanowires, which interfaced with the TiO₂ nanotubes in the 1st-set pores. Finally, TiO₂-nanotubes/Au-nanowires arrays were obtained after dissolving the AAO template in NaOH solutions (S14 and S15).

SEM and FIB cutting. All scanning electron microscope (SEM) analysis of structural morphology and nanoscale cutting in this work were performed by Focused Ion Beam Scanning Electron Microscopes (FIB-SEMs, ZEISS).

SERS measurement. The preparation for surface-enhanced Raman spectroscopy (SERS) measurement was performed by immersing arrays of in-plane shape-different Ag nanoparticles into Rhodamine 6G aqueous solutions with a concentration of 10^{-6} M. The immersion procedure was carried out for 4 hr to assure that sufficient R6G molecules can be chemisorbed on the surface of Ag nanoparticles, especially the hot spots under electromagnetic excitation (namely, the vertices of triangular nanoparticles). Before measurement, all samples were dipped into DI water for 30 sec and dried with nitrogen flow. SERS signals spectra with three main peaks at 1363, 1508, and 1650 cm^{-1} were collected by the NTEGRA Spectra system (NTMDT) equipped with a laser source of 532-nm wavelength. The measured data were treated with baseline correction to extract SERS spectra from the broad background.

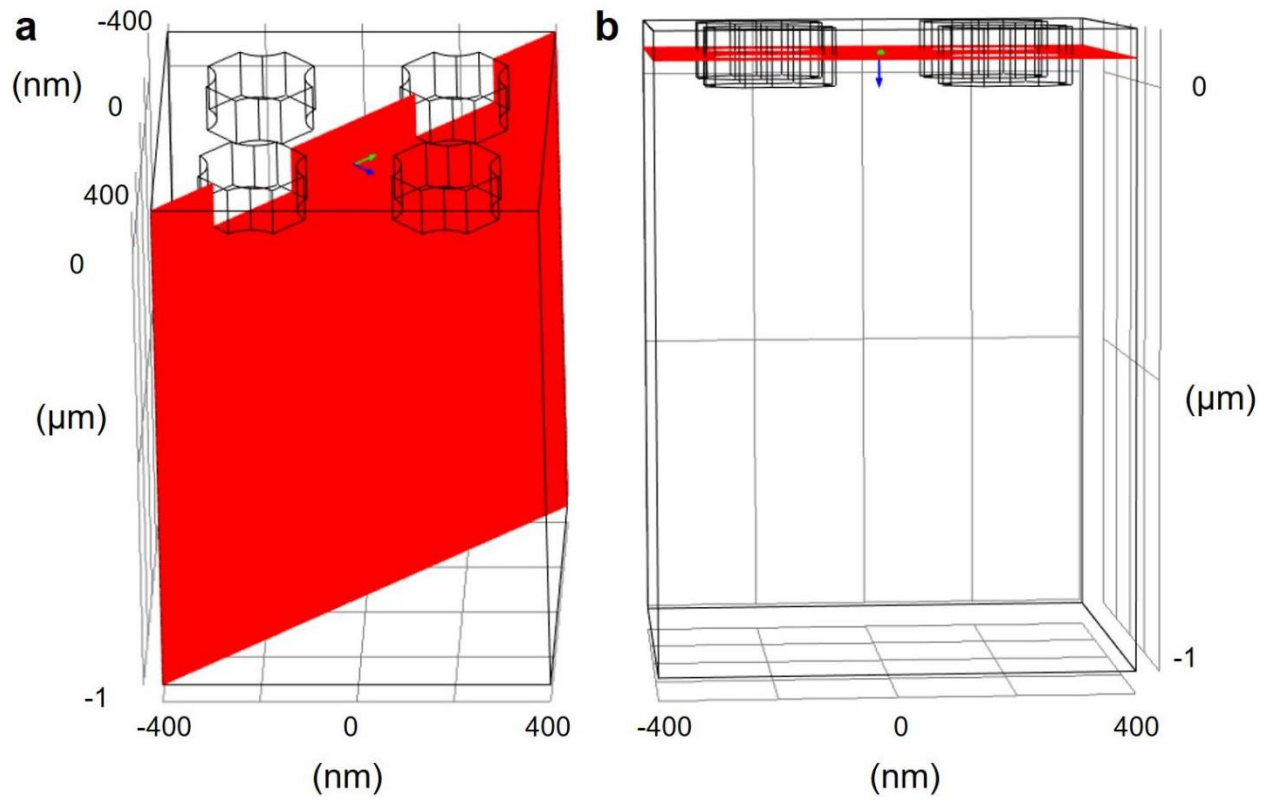
Optical measurement. UV-vis-NIR spectrometer (Varian Cary 5000) was exploited to characterize light trapping performance. All optical measurements were performed with an illumination spot size of approximately 20 mm^2 at normal incidence without polarization. Considering opaqueness for all samples, the experimental light absorption spectra in this work were calculated by $100\% - R\%$ where $R\%$ represents the light reflection efficiency.

Photoelectrocatalytic measurement. The hydrogen production was measured by a gas chromatography analyzer (Agilent Micro-GC). For facilitating redox reaction, Pt nanoparticles were formed at the surface of TiO_2 nanotubes by ALD. The photocatalysts of TiO_2 nanotubes and Au-nanowires/ TiO_2 -nanotubes combinations were immersed into a mixture solution of 1:4 v/v methanol/DI water. Argon-flow purging was kept for 1 hr to eliminate the dissolved oxygen from the aqueous solution. During measurement, the photocatalytic samples were illuminated by simulated AM 1.5G solar spectrum or visible light with a 420-nm long-pass filter. The hydrogen production rates for all samples were normalized to the corresponding active areas.

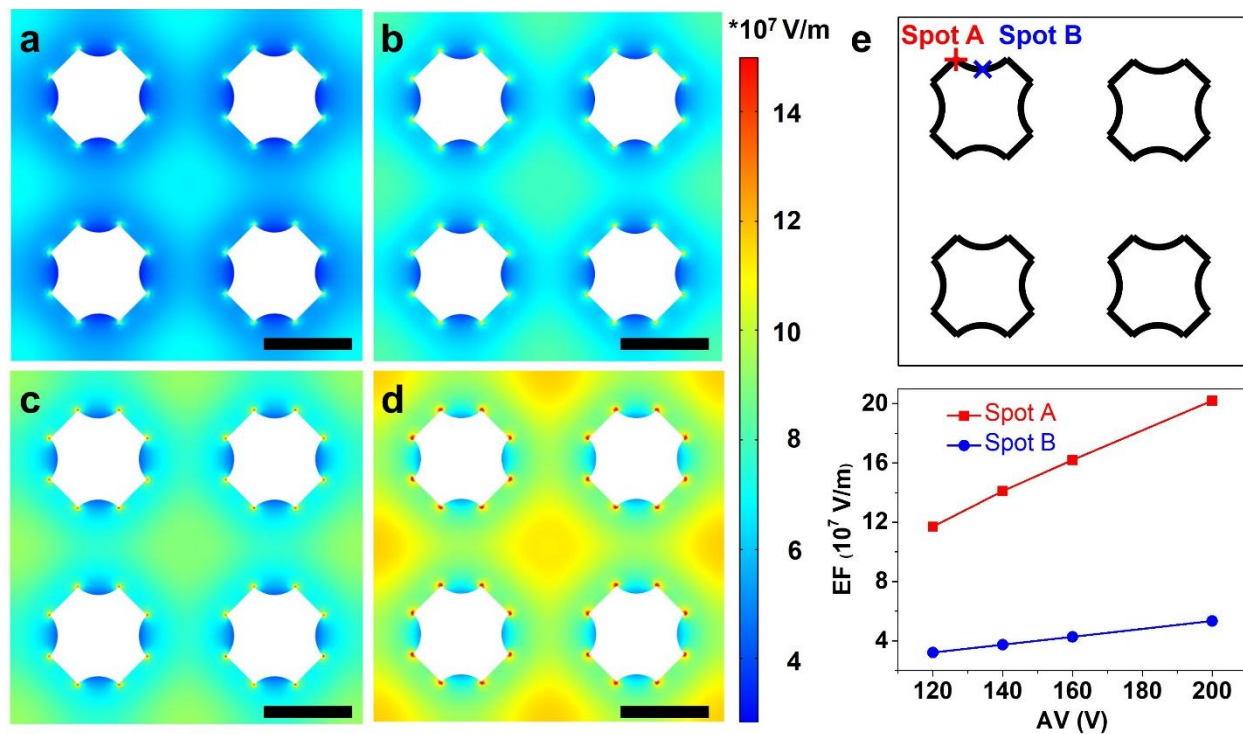
COMSOL simulation. To characterize the electric field distribution in aluminium foils at the initial stage of anodization, we exploited the ACDC module (simple resistor) from COMSOL Multiphysics (5.1 version) for simulation. The geometrical features of surface-patterned aluminium foils exploited in simulation were set according to the experimental observation. Quadruple and sextuple unit cells with periodic boundary conditions were exploited for calculation, corresponding to the experimental nanodents of tetragonal and hexagonal arrangements, respectively. A voltage difference was applied between the top surface and bottom of the aluminium foil to simulate the external AV.

FDTD simulation. Optical simulations were performed with a commercial software package (FDTD solutions, Lumerical Solutions). Three-dimensional layouts were exploited for all numerical calculations. The plane-wave light source propagating in the $-z$ direction was used to illuminate nanostructure arrays, which were situated on a substrate parallel with the xy plane. Periodic boundary condition was set along the x and y directions, and perfectly matched layers were used to cut the z axis. The geometries of nanostructure arrays in simulation were measured from the corresponding SEM images. The electric field maps were recorded by two-dimensional

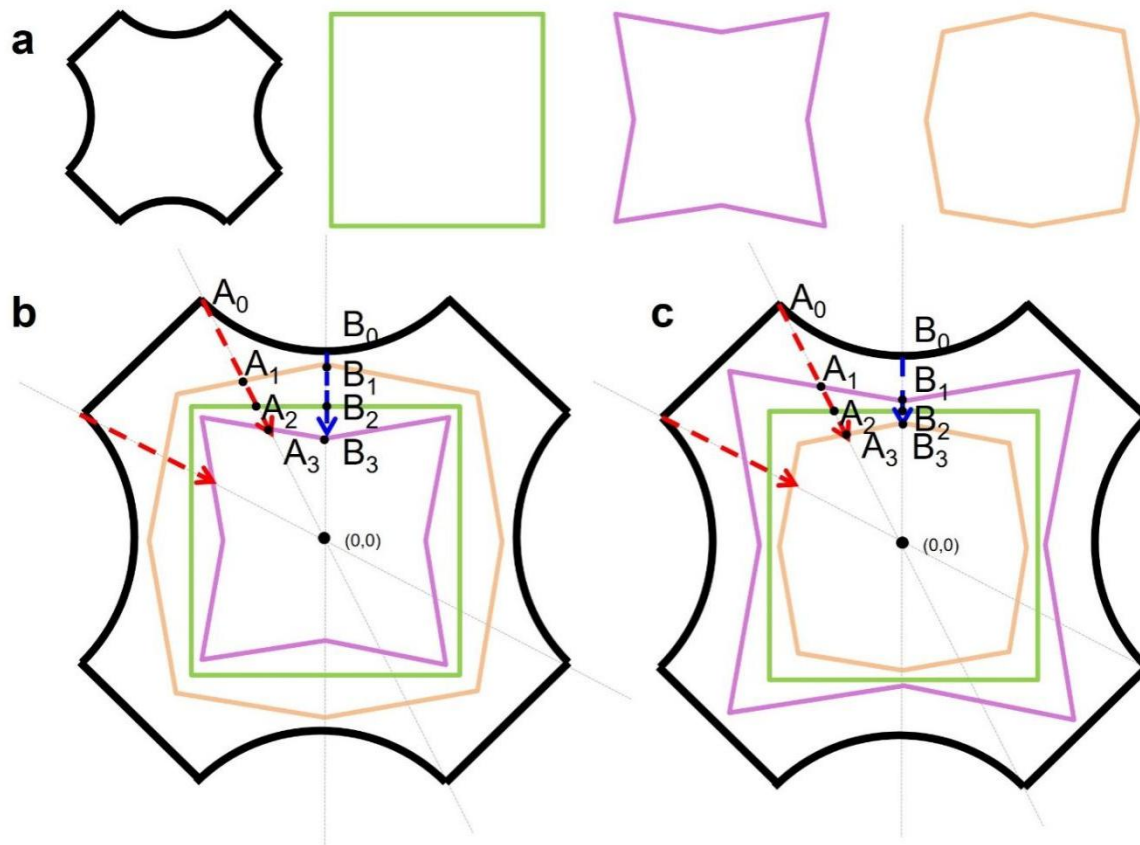
frequency-domain field profile monitors. For calibrating the light absorption efficiencies ($A\%$), two two-dimensional power monitors were exploited: one was placed at the bottom of the nanostructure array to measure the transmitted power ($T\%$), and the other was located above the light source to measure the reflected power ($R\%$). The light absorption spectra were obtained by $100\% - T\% - R\%$. Optical properties of Ag and Au in simulation were obtained from Johnson and Christy¹, and optical data reported in Siefke's paper were used for modeling TiO_2 ².



Supplementary Fig. 1 | Three-dimensional layout of surface-patterned aluminium foil in COMSOL simulation. (a) Vertical cross section and (b) near-surface lateral cross section, cutting through the nanodents in an aluminium foil.



Supplementary Fig. 2 | COMSOL-simulated electric field maps over the near-surface lateral cross section of surface-patterned aluminium foil at different AVs. Electric field maps at the AVs of (a) 120 V, (b) 140 V, (c) 160 V, and (d) 200 V. For a clear comparison, the color bars of all electric field maps are set to be identical. The electric field map in (a) is derived from (and same as) that in Fig. 1b. Scale bars: 200 nm. (e) Schematic illustration of 2×2 nanodent array and the electric fields at spot A and spot B as a function of AV.



Supplementary Fig. 3 | Schematic illustration of pore shape evolution for imprinted nanodents during anodization. (a) The black polygon represents a nanodent on the aluminium foil surface. The green square, the pink square with internally-bent walls, and the orange square with externally-bent walls are possible shapes of anodized pores, featuring fourfold symmetry. (b,c) Two possible trends of pore shape evolution as a function of AV. In (b), increasing AV leads to the pore shape alteration from the square with externally-bent walls to the square without bending walls and then the square with internally-bent walls; in (c), the pore shape is altered from the square with internally-bent walls to the square without bending walls and then the square with externally-bent walls. The red arrow marks the expansion pathways for two representative points (A_0 and B_0) as increasing AV. Two points have the maximum and the minimum electric fields along the nanodent wall, respectively (Supplementary Fig. 2).

Given that the nanodent shape and the corresponding electric field maps (Supplementary Fig. 2) are characterized by fourfold symmetry, the anodized pores will thus inherit the identical structural symmetry as the nanodent. The possible pore shapes featuring fourfold symmetry can be roughly categorized into three types: the square without bending walls, the square with internally-bent walls, and the square with externally-bent walls, as summarized in Supplementary Fig. 3a.

As previously reported, acid anions such as PO_4^{3-} are driven into the oxide layer during anodization, and the number of incorporated acid anions is positively related to the volume

expansion^{3,4}. Given that the A_0 point is always higher than the B_0 position in electric field (Supplementary Fig. 2), more acid anions will be incorporated into the A_0 point, leading to larger volume expansion than the B point. In particular, the AV increase from 120 V to 200 V also leads to greater electric field difference between the A_0 point and the B_0 point (Supplementary Fig. 2), which consequently causes larger volume expansion difference. As a result, the pore shape evolution as a function of AV shown in Supplementary Fig. 3b is not correct because its volume expansion difference gets reduced with the AV increase, namely,

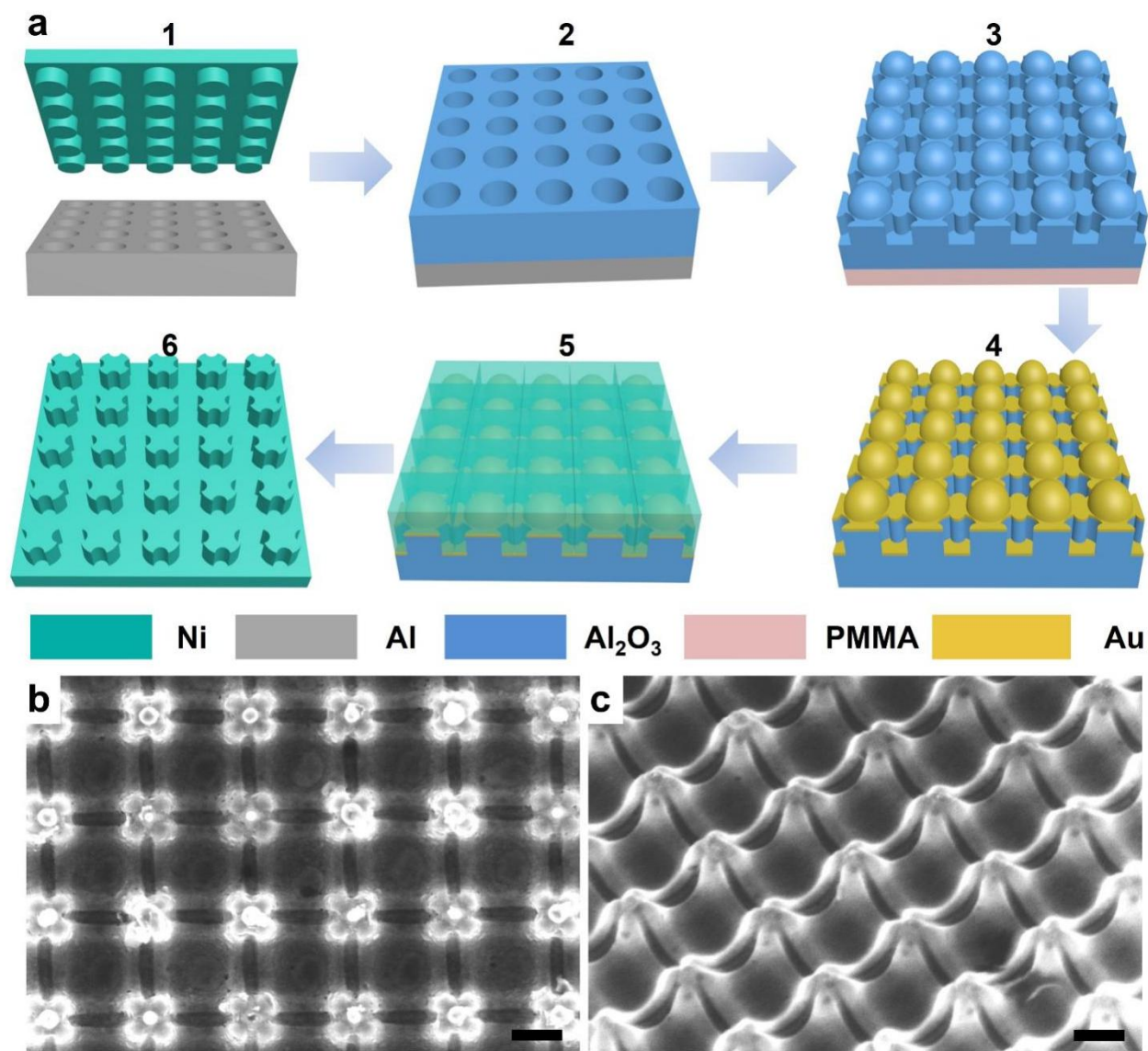
$$\frac{A_0 \rightarrow A_1}{B_0 \rightarrow B_1} > \frac{A_0 \rightarrow A_2}{B_0 \rightarrow B_2} > \frac{A_0 \rightarrow A_3}{B_0 \rightarrow B_3}$$

where $X_i \rightarrow X_j$ is the distance between the point X_i and the point X_j .

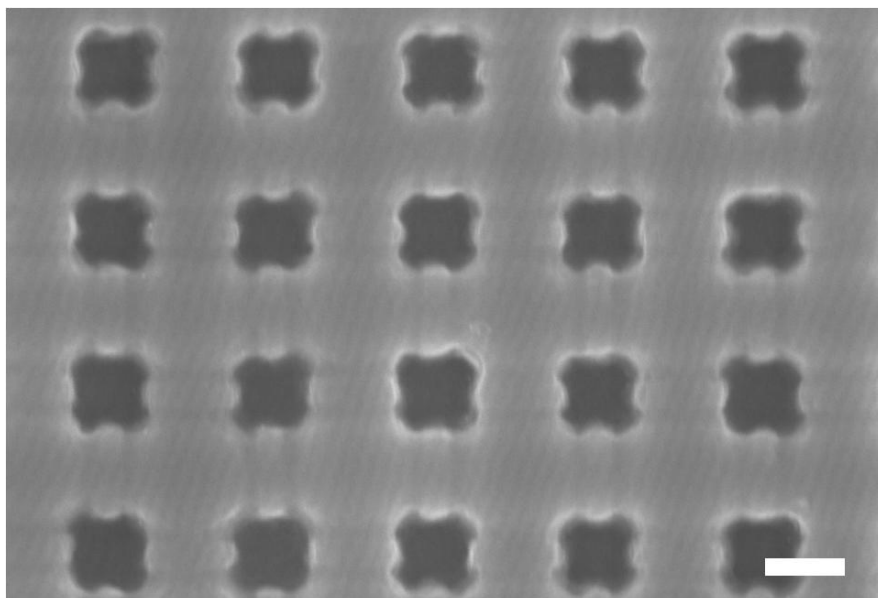
Therefore, with the AV increase the pore shape should be altered from square with internally-bent walls to square without bending walls and then square with externally-bent walls, as schematically illustrated in Supplementary Fig. 3c. In such an alteration, the volume expansion difference between the points A and B is gradually enhanced, that is,

$$\frac{A_0 \rightarrow A_1}{B_0 \rightarrow B_1} < \frac{A_0 \rightarrow A_2}{B_0 \rightarrow B_2} < \frac{A_0 \rightarrow A_3}{B_0 \rightarrow B_3}$$

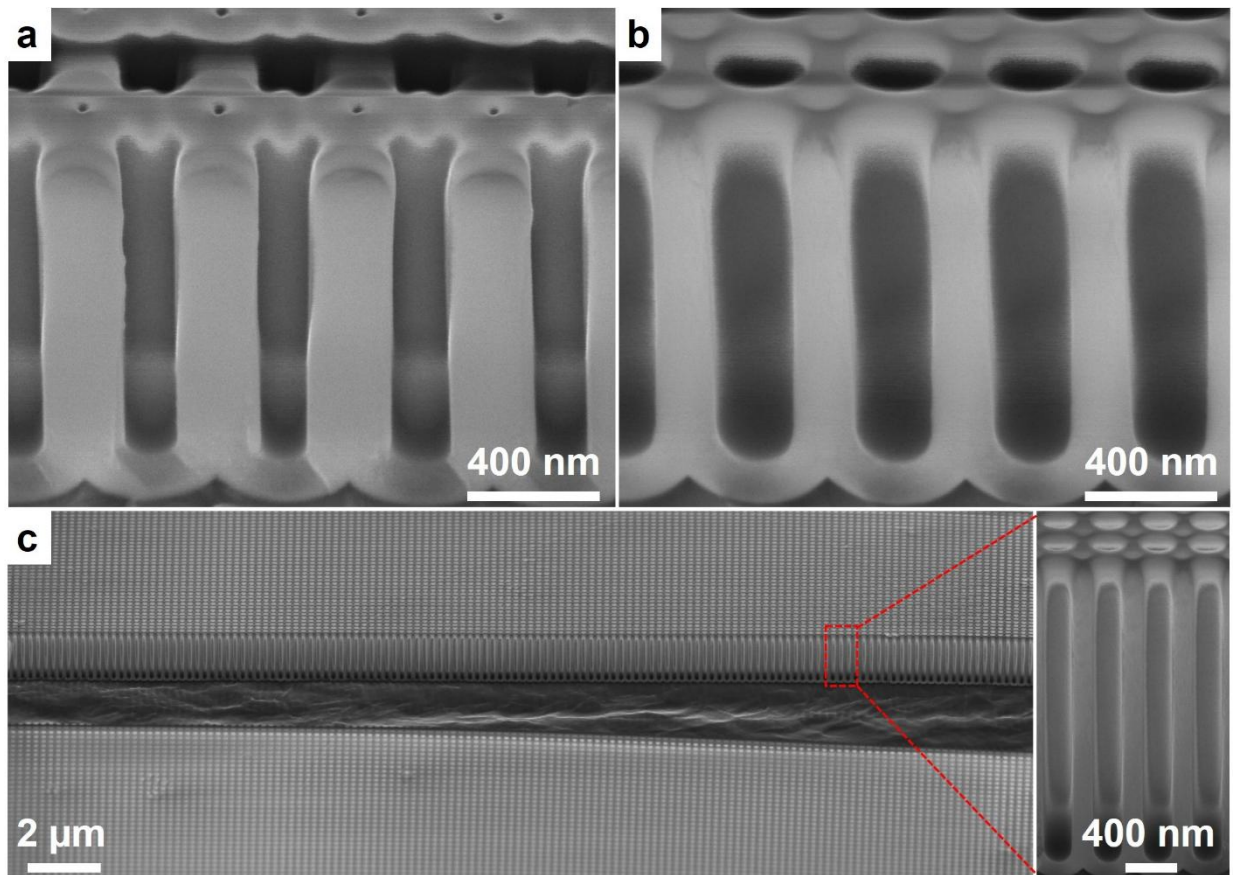
Accordingly, it is envisaged that higher AVs lead to smoother and more externally-bent walls and lower AVs lead to sharper and more internally-bent walls.



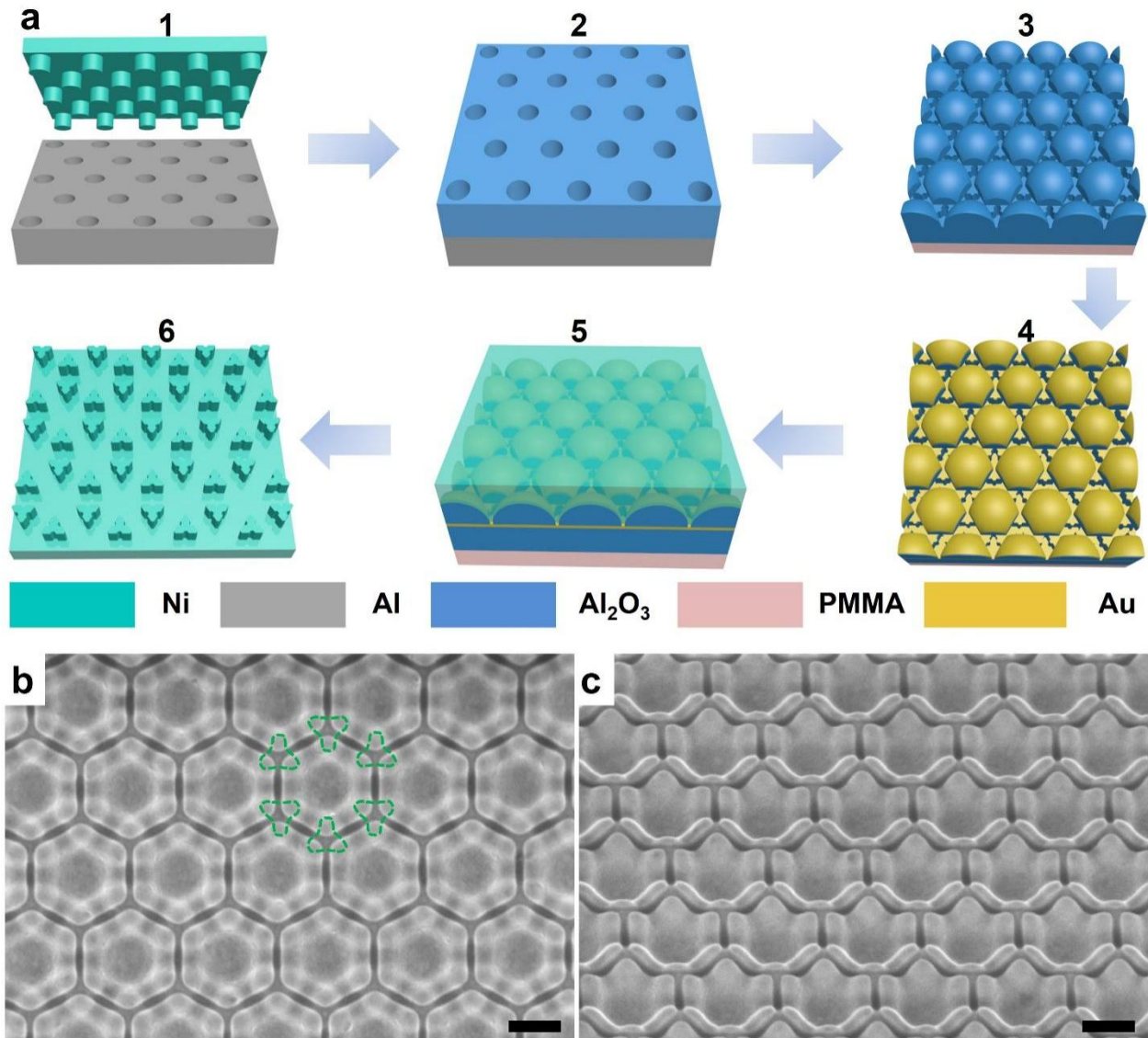
Supplementary Fig. 4 | Fabrication of Ni imprint stamp decorated with four-leaf clover-like nanopillars. (a) Schematic illustration of the fabrication process: (1) Imprinting aluminium foil using Ni stamp with a tetragonal array of circular nanopillars; (2) Anodic anodization; (3) Coating PMMA over the anodized area, followed by removing the unanodized aluminium and selectively etching the bottom surface of the anodized template; (4) Evaporating Au by PVD to form a conductive layer; (5) Performing Ni electrodeposition to replicate the as-etched shape of the bottom surface; (6) Dissolving PMMA and removing AAO template. (b) Top- and (c) tilted-view SEM images of Ni imprint stamp with four-leaf clover-like nanopillars. Because the tetragonal array of Ni nanopillars exploited in step 1 is 400 nm in spacing, the resultant array of four-leaf clover-like nanopillars obtained in step 6 is 400 nm as well. Scale bars: 200 nm.



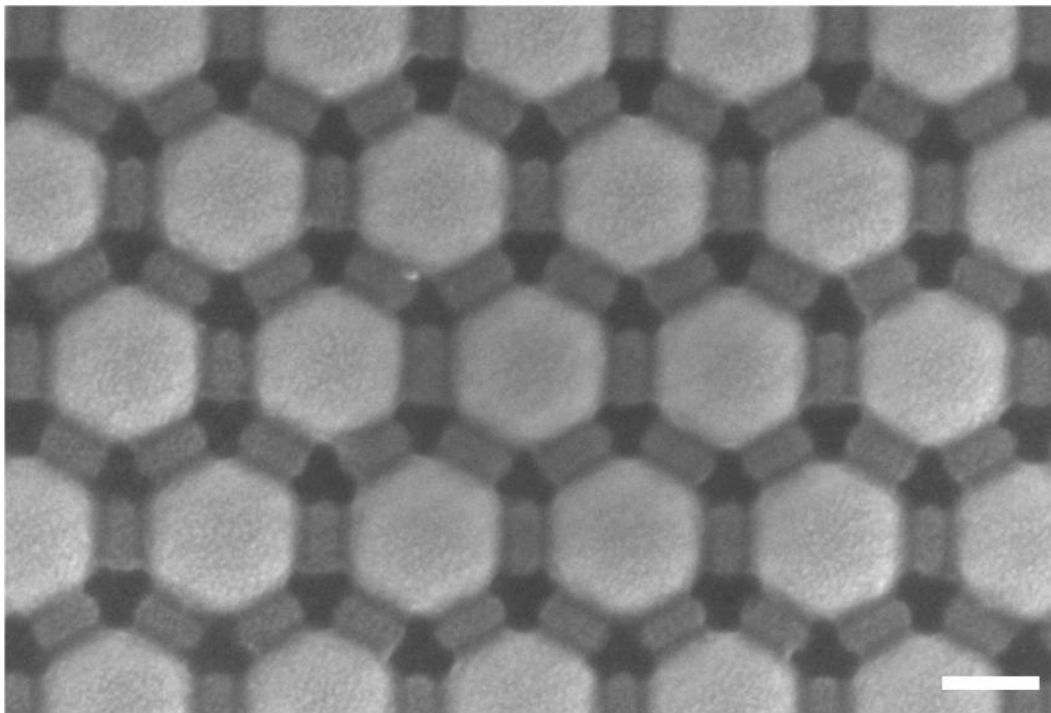
Supplementary Fig. 5 | Aluminium foil with a tetragonal array of four-leaf clover-like nanodents. Scale bar: 200 nm.



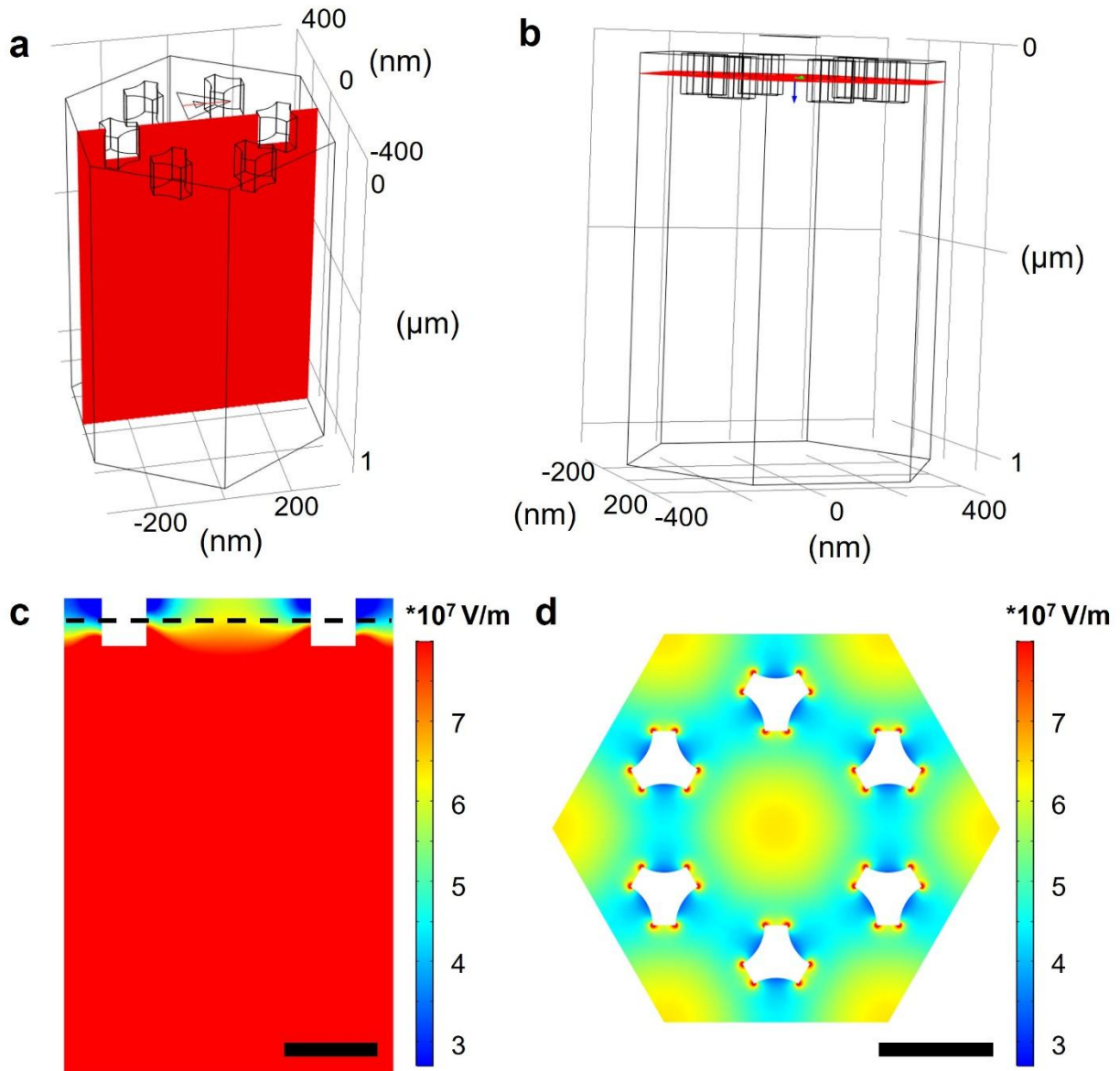
Supplementary Fig. 6 | Cross-sectional SEM images of tetragonally arranged nanopores anodized at different AVs. Anodization was carried out at (a) 120 V and (b,c) 200 V. For clearly showing the circular shape, pore-widening in NaOH solutions was performed upon the samples in (b,c).



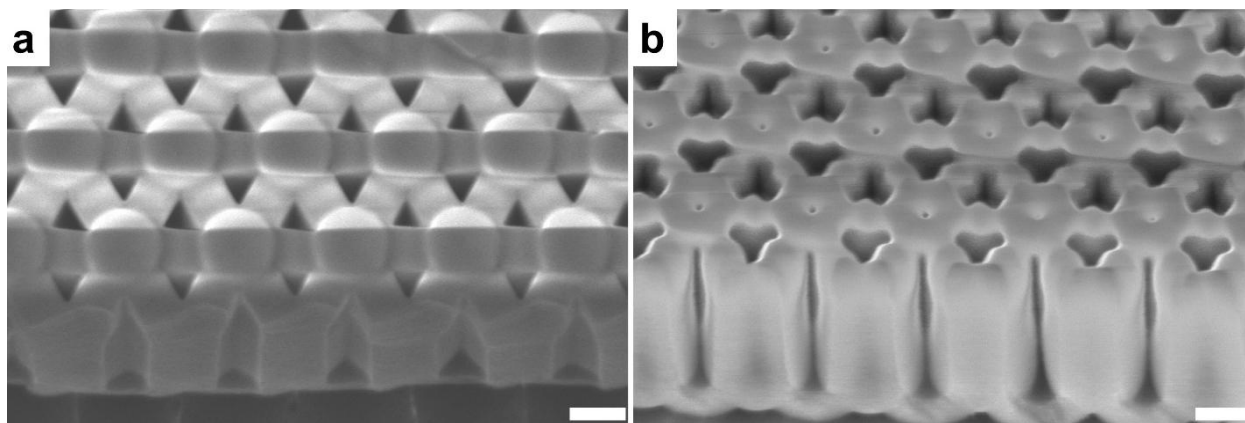
Supplementary Fig. 7 | Fabrication of Ni imprint stamp decorated with three-leaf clover-like nanopillars of hexagonal arrangement. (a) Schematic illustration for fabrication process. (b) Top-view and (c) tilted-view SEM images of Ni imprint stamp with three-leaf clover-like nanopillars. The shapes of nanopillars are outlined by green dashed lines in (b). Because the trigonal array of nanopillars anchored on the original Ni imprint stamp exploited in step 1 is 400 nm in spacing, the resultant hexagonal array of three-leaf clover-like nanopillars obtained in step 6 is $400/\sqrt{3}$ nm. Scale bars: 200 nm.



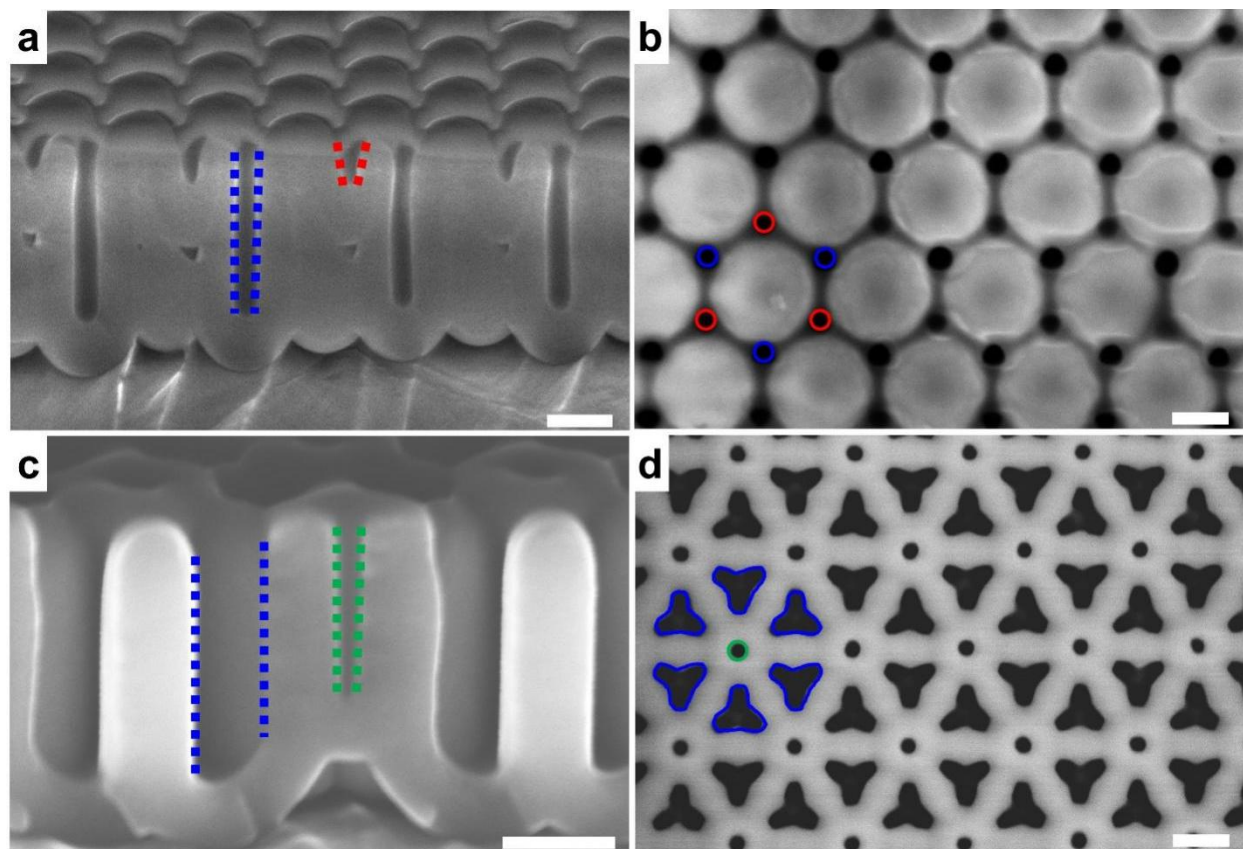
Supplementary Fig. 8 | Surface-patterned aluminium foil with a hexagonal array of three-leaf clover-like nanodents. Scale bar: 200 nm.



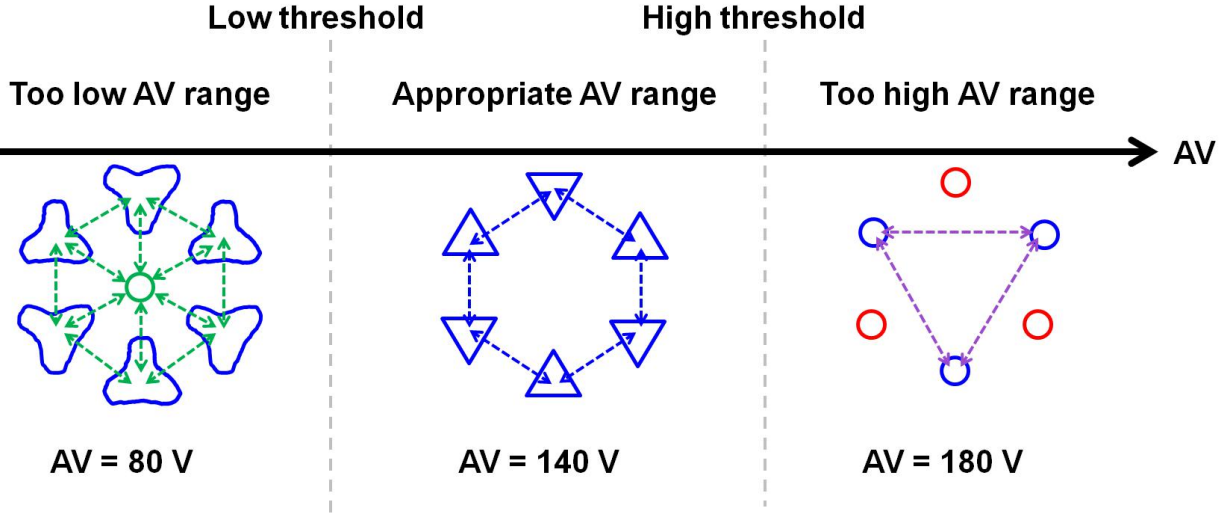
Supplementary Fig. 9 | Simulation of electric field maps in an aluminium foil engineered with a hexagonal array of three-leaf clover-like nanodents at the initial stage of anodization. (a) Vertical cross section and (b) near-surface lateral cross section of three-dimensional surface-patterned aluminium foil. Simulated electric field maps under an AV of 100 V at the (c) vertical cross section and (d) near-surface lateral cross section. The dashed line in (c) at the half-depth of nanodents indicates the near-surface lateral cross section in (d). Scale bars: 200 nm.



Supplementary Fig. 10 | Cross-sectional SEM images of hexagonally arranged nanopores anodized at different AVs. Anodization was carried out at (a) 140 V and (b) 100 V, respectively. Scale bars: 200 nm.



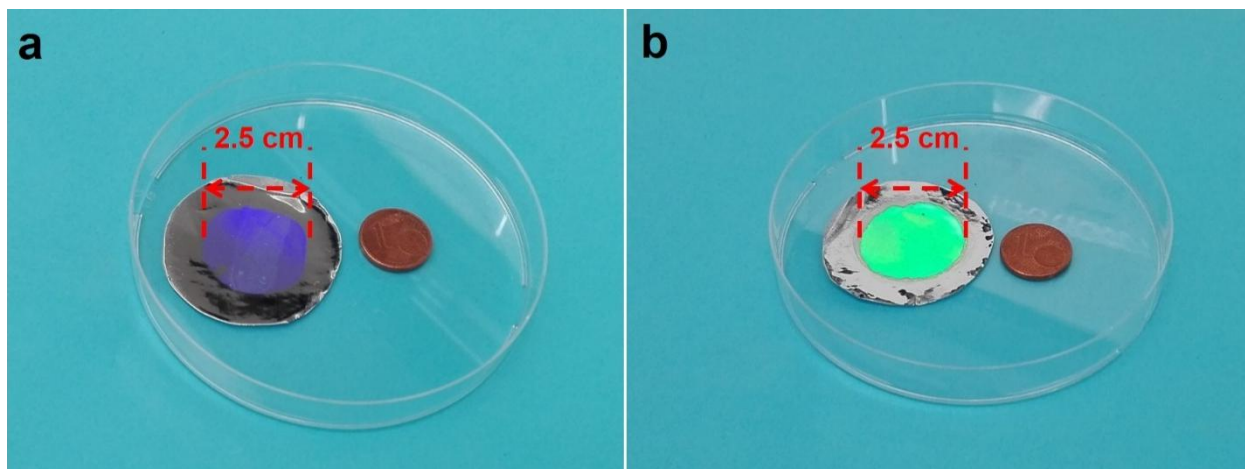
Supplementary Fig. 11 | AAO templates obtained by anodizing aluminium foil with a hexagonal array of three-leaf clover-like nanodents in a broad AV range. (a) Cross-sectional-view and **(b)** top-view SEM images of an AAO template anodized at 180 V, showing that within a hexagonal unit of six pores, three diagonally neighboring pores (red-colored) disappear, leaving only very shallow nanodents on the top of the template. **(c)** Cross-sectional-view and **(d)** top-view SEM images of an AAO template anodized at 80 V, showing that a new pore (green-colored) was formed at the junction site of six adjacent pores. Scale bars: 200 nm.



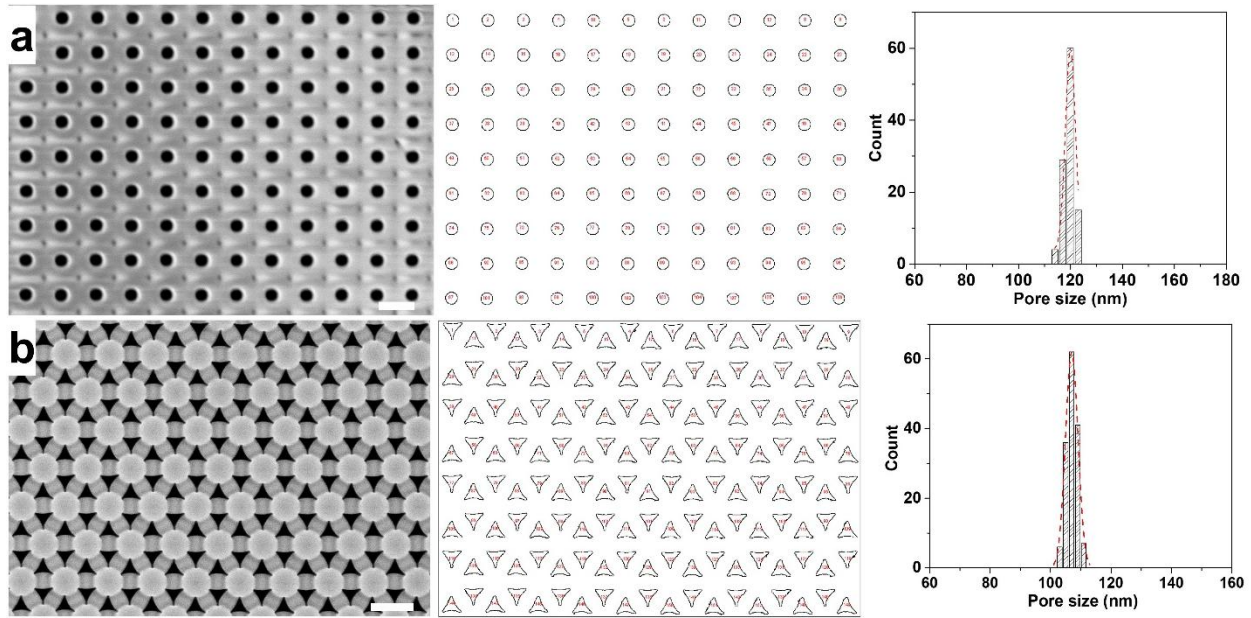
Supplementary Fig. 12 | Pore arrangement after anodization at different AVs. Here we select the hexagonal array of nanodents as an example and demonstrate three representative pore arrangements after anodization with the AVs of 80, 140, and 180 V.

Based on the experimental results shown in Fig. 1h-k and Supplementary Fig. 11, it can be concluded that the AVs for a specific array of nanodents should be divided into three ranges: too low AV range, appropriate AV range, and too high AV range. For appropriate AVs, the pore arrangement (e.g., the hexagonal arrangement depicted by blue dashed arrows) predetermined by imprinting can remain during anodization; for too high AVs, the predetermined arrangement was destroyed due to the disappearance of diagonally neighboring red pores, forming a new trigonal arrangement (depicted by purple dashed arrows); for too low AVs, the pre-set arrangement was also destroyed with the occurrence of a green pore at the center of a unit cell (i.e., the junction site of six adjacent blue-colored pores), giving rise to another trigonal arrangement (depicted by green dashed arrows).

In general, the three ranges are separated by two threshold values, as schematically illustrated in Supplementary Fig. 12. Its two thresholds are empirically observed to be V_a and $\sqrt{3} V_a$, where $V_a = 0.4 \text{ nm/V} \times L_h$ and L_h is the interpore spacing of the hexagonal array (i.e., $400/\sqrt{3} \text{ nm}$). In other words, AV thresholds can be derived from the linear spacing-AV relation, i.e., $\text{AV (V)} = \text{spacing (nm)} \times 0.4 \text{ (V/nm)}$ or $\text{spacing (nm)} = \text{AV (V)} \times 2.5 \text{ (nm/V)}$ ⁵, regarding two spacings (e.g., L_h and $\sqrt{3}L_h$) of emerging arrays.



Supplementary Fig. 13 | Optical photographs of surface-patterned aluminium foils (a) before and (b) after anodization.

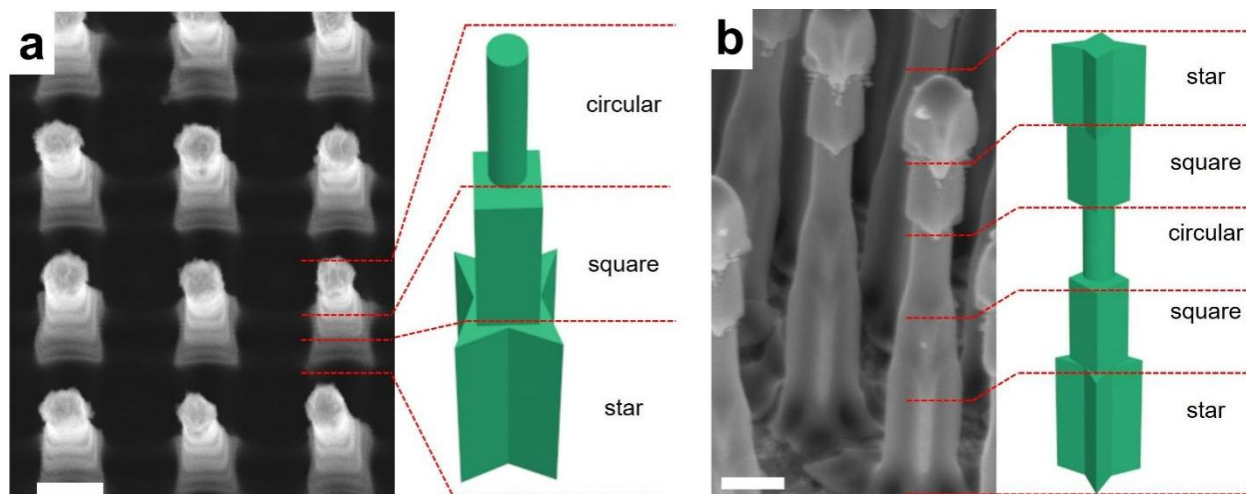


Supplementary Fig. 14 | Nearly monodisperse pore size distribution of AAO template. Pores are arrayed in (a) tetragonal and (b) hexagonal arrangements. Scale bars: 400 nm.

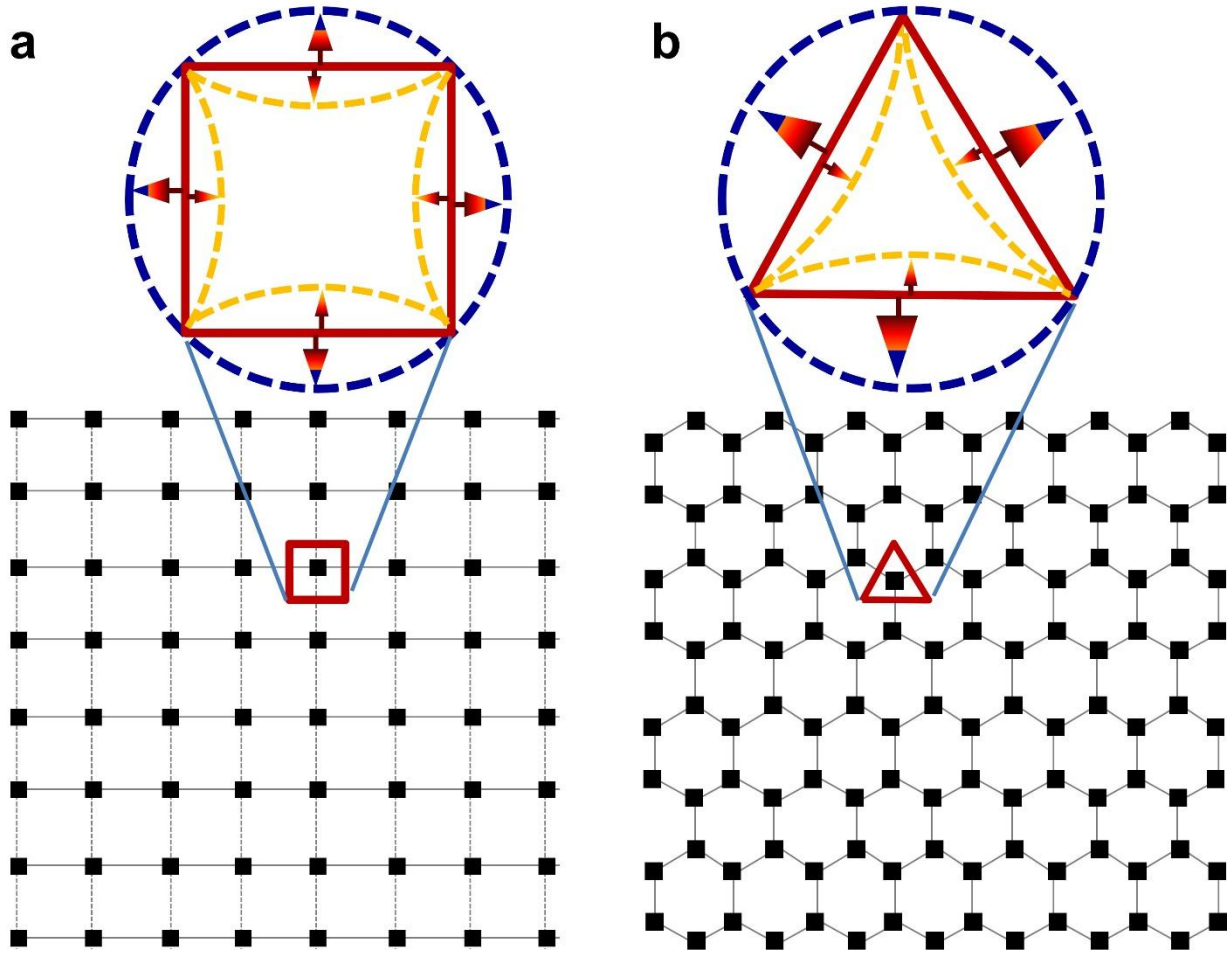
Given the shape diversity for pores in AAO templates, especially for those with bent walls, there is a lack of a universal parameter to evaluate pore size. For quantitative comparison, the pore size (*Size*) in this work was calculated by

$$Size = \sqrt{area} \quad (1)$$

Statistical analysis of pore area (*area*) was performed with open-source software ImageJ (downloaded from <https://imagej.nih.gov/ij/index.html>). The slight deviation was mostly ascribed to the geometrical dispersion of the lab-made Ni nanopillars and should be avoided using standard imprint stamps.



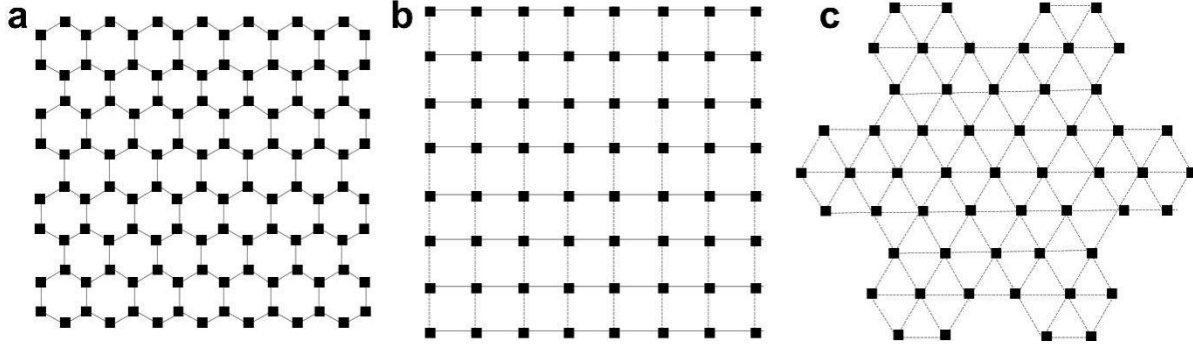
Supplementary Fig. 15 | TiO_2 multi-segment nanowires. (a) Tilted-view SEM image and schematic illustration for three-segment nanowires (from bottom to top: star+square+circular), replicated from an AAO template with three-segment pores (sequentially anodized at $140 \rightarrow 160 \rightarrow 200$ V). (b) Tilted-view SEM image and schematic illustration for five-segment nanowires (from bottom to top: star+square+circular+square+star), replicated from an AAO template with five-segment pores (sequentially anodized at $140 \rightarrow 160 \rightarrow 200 \rightarrow 160 \rightarrow 140$ V). Scale bars: 200 nm.



Supplementary Fig. 16 | Shape tuning trend (up) of AAO pores in a specific spatial configuration (down). The black dots represent the central sites of pores in the corresponding arrangements. The blue, red, and yellow polygons schematically outline the pore shapes anodized at different AVs.

(a) In the tetragonal arrangement, the pore can be evolved from the square shape to the wall-externally-bent square shape by increasing AV or to the wall-internally-bent square shape by decreasing AV. (b) In the hexagonal arrangement, the pore shape can be evolved from the triangular shape to the wall-externally-bent triangular shape by increasing AV or to the wall-internally-bent triangular shape by decreasing AV.

In general, the walls of the as-anodized pores are always perpendicular to the lines that link the central sites of two adjacent pores. That is to say, the pore shape in term of structural symmetry is highly dependent on the spatial configuration of neighboring pores.



Supplementary Fig. 17 | Tessellation of a two-dimensional plane using regular polygons: (a) hexagon, (b) tetragon, and (c) trigon. The black dots represent the central sites of pores in the corresponding arrangements.

If a tessellation is tiled without gap by only one regular polygon, the corners of the polygon need to fit into each other around a point, meaning that 360° must be evenly divided by the corner angle (β) of the regular polygon:

$$\frac{360^\circ}{\beta} = n \quad (2)$$

where n are integers (e.g., 1, 2, 3...).

For the regular polygon including m sides, the corner angle β can be described by the following equation:

$$\beta = \frac{(m-2) \times 180^\circ}{m} = 180^\circ - \frac{360^\circ}{m} \quad (3)$$

Because of $m \geq 3$, the corner angle β is never less than 60° .

Based on the above recognition, we can conclude that:

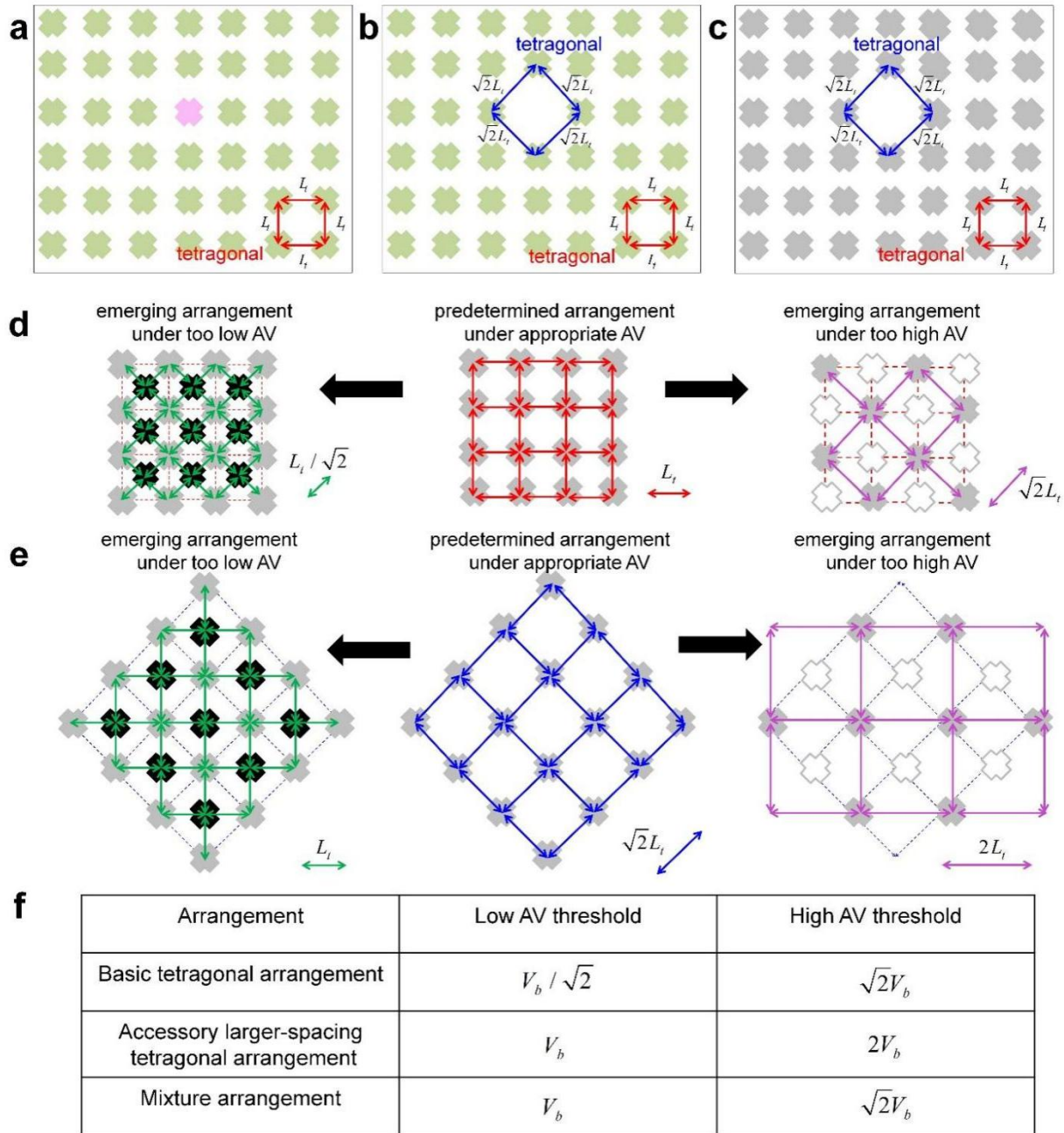
(i) when $n = 3$, $\beta = 120^\circ$, $3 \times 120^\circ = 360^\circ$, there is a tessellation using three regular hexagons around each vertex, corresponding to the hexagonal arrangement shown in Supplementary Fig. 17a;

(ii) when $n = 4$, $\beta = 90^\circ$, $4 \times 90^\circ = 360^\circ$, there is a tessellation using four regular tetragons around each vertex, corresponding to the tetragonal arrangement shown in Supplementary Fig. 17b;

(iii) when $n = 6$, $\beta = 60^\circ$, $6 \times 60^\circ = 360^\circ$, there is a tessellation using six regular trigons around each vertex, corresponding to the trigonal arrangement shown in Supplementary Fig. 17c.

(iv) if n is further increased (e.g., $n = 9, 12, 18$), the corner angle β (e.g., $40^\circ, 30^\circ, 20^\circ$) will be less than 60° .

Therefore, only three regular polygons (i.e., trigon, tetragon, and hexagon) can tile a two-dimensional plane without gap.



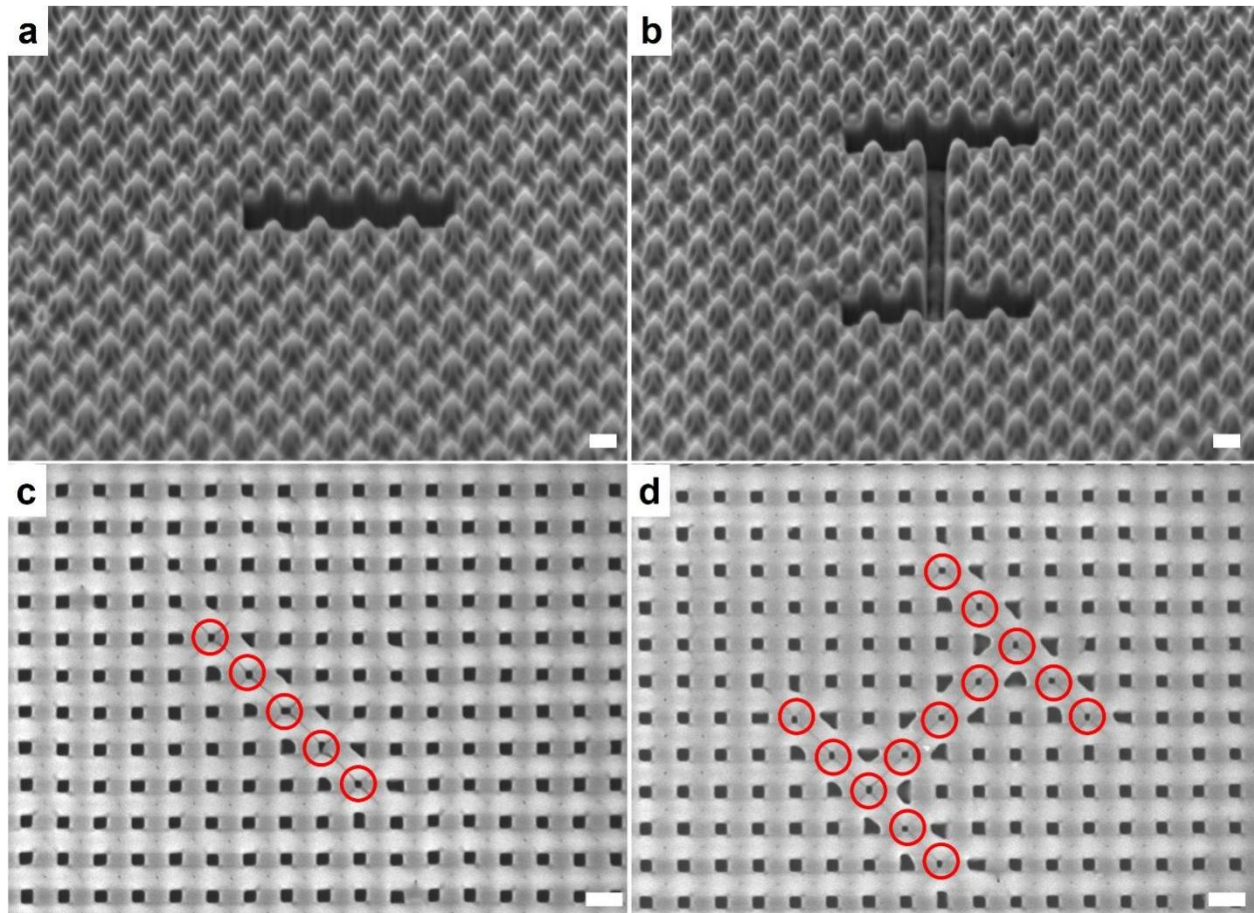
Supplementary Fig. 18 | Pore arrangement evolution of surface-patterned aluminium foil with spacing-different tetragonal arrangements under different AVs. Schematic illustrations for (a) imprint stamp of L_T -spacing tetragonal arrangement and (b) imprint stamp equipped with two tetragonal arrangements of different spacings (i.e., L_T and $\sqrt{2}L_T$), $L_T = 400$ nm. For obtaining the imprint stamp in (b), a nanopillar marked by pink color in (A) was removed by using Zeiss FIB-SEMs system. (c) Surface-patterned aluminium foil using imprint stamp in (B). Pore arrangement evolution of (d) basic L_T -spacing tetragonal arrangement and (e) accessory $\sqrt{2}L_T$ -spacing tetragonal arrangement under too low AVs, appropriate AVs, and too high AVs. The

pores shown in (d) and (e) are just for demonstration of pore arrangement and do not represent the real pore shapes. The gray cross, black cross, and hollow cross demonstrate the pores occurring at the site of predetermined nanodent, the emerging pores, and the disappearing pores from the sites of predetermined nanodent, respectively. (f) Appropriate AV ranges for the basic L_r -spacing tetragonal arrangement, the accessory $\sqrt{2}$ L_r -spacing tetragonal arrangement and the mixture arrangement.

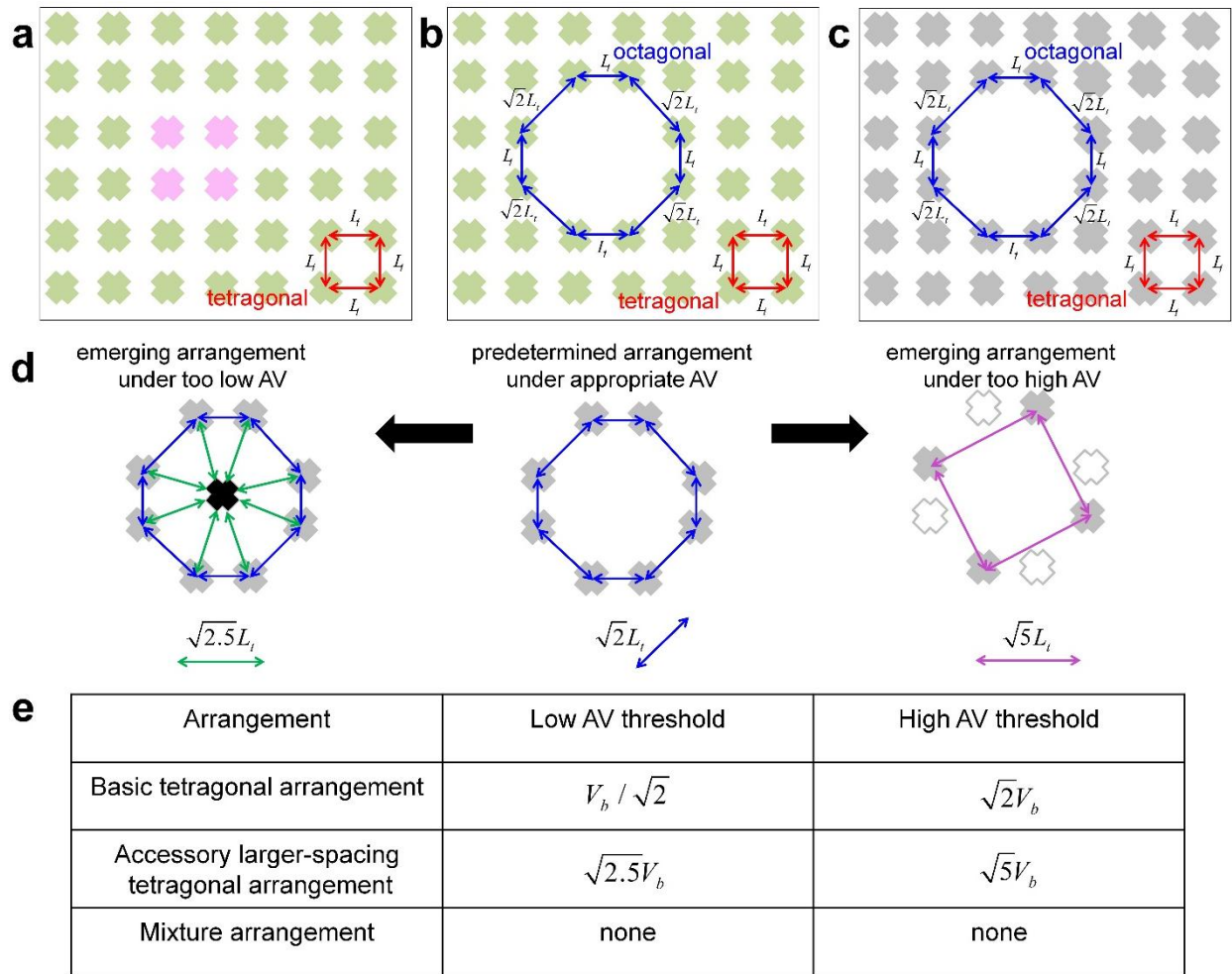
As stated in Supplementary Fig. 12, the appropriate AV range for a specific arrangement should have two thresholds which are derived from the linear spacing-AV relation regarding two spacings of emerging arrays⁵. To prevent the disappearance of diagonally neighboring pores during anodization for the L_r -spacing arrangement (middle part of Supplementary Fig. 18d), the appropriate AVs should be lower than $\sqrt{2} V_b$ (that is, the high AV threshold defined by $0.4 \text{ V/nm} \times \sqrt{2} L_t$), where V_b corresponds to the conventional AV for the L_r -spacing arrangement and is defined by $0.4 \text{ V/nm} \times L_t$. And $\sqrt{2} L_t$ indicates the spacing of emerging arrangement (depicted by pink arrows) after the disappearance of diagonally neighboring pores from the L_r -spacing arrangement under too high AVs, as shown in the right part of Supplementary Fig. 18d. Similarly, the appropriate AVs for the $\sqrt{2} L_r$ -spacing arrangement should be lower than $2 V_b$ (that is, the high AV threshold defined by $0.4 \text{ V/nm} \times 2L_t$). And $2L_t$ indicates the spacing of emerging arrangement (depicted by pink arrows) after the disappearance of diagonally neighboring pores from the $\sqrt{2} L_r$ -spacing arrangement under too high AVs, as shown in the right part of Supplementary Fig. 18e.

Furthermore, to prevent the occurrence of new pores at the central site of a tetragonal unit during anodization for the L_r -spacing arrangement, the appropriate AVs for the L_r -spacing arrangement should be higher than $V_b/\sqrt{2}$, that is, the low AV threshold defined by $0.4 \text{ V/nm} \times L_t/\sqrt{2}$, where $L_t/\sqrt{2}$ indicates the spacing of emerging arrangement (depicted by green arrows) after the occurrence of new pores in the L_r -spacing arrangement under too low AVs, as shown in the left part of Supplementary Fig. 18d. Similarly, the appropriate AVs for the $\sqrt{2} L_r$ -spacing arrangement should be higher than V_b , that is, the high AV threshold defined by $0.4 \text{ V/nm} \times L_t$. And L_t indicates the spacing of emerging arrangement (depicted by green arrows) after the occurrence of new pores in the $\sqrt{2} L_r$ -spacing arrangement under too low AVs, as shown in the left part of Supplementary Fig. 18e.

In theory, the appropriate AV ranges for two arrangements should be $(V_b/\sqrt{2}, \sqrt{2} V_b)$ and $(V_b, 2 V_b)$, respectively. Thus, the intersectional AV range for the mixture arrangement should be from V_b (160 V) to $\sqrt{2} V_b$ (~226 V).



Supplementary Fig. 19 | Anodization upon surface-patterned aluminium foils with two spacing-different arrangements. (a,b) Several nanopillars in Ni perfect stamps were removed by Zeiss FIB-SEMs system to combine two arrangements in one matrix. Because the spacing of the basic arrangement is $L_t = 400$ nm, the new arrangement has the spacing of $\sqrt{2} L$. After performing anodization at 158 V, small pores were still obtained at the deficiency sites without nanodents, as observed in (c,d) SEM images of AAO templates. Scale bars: 400 nm.

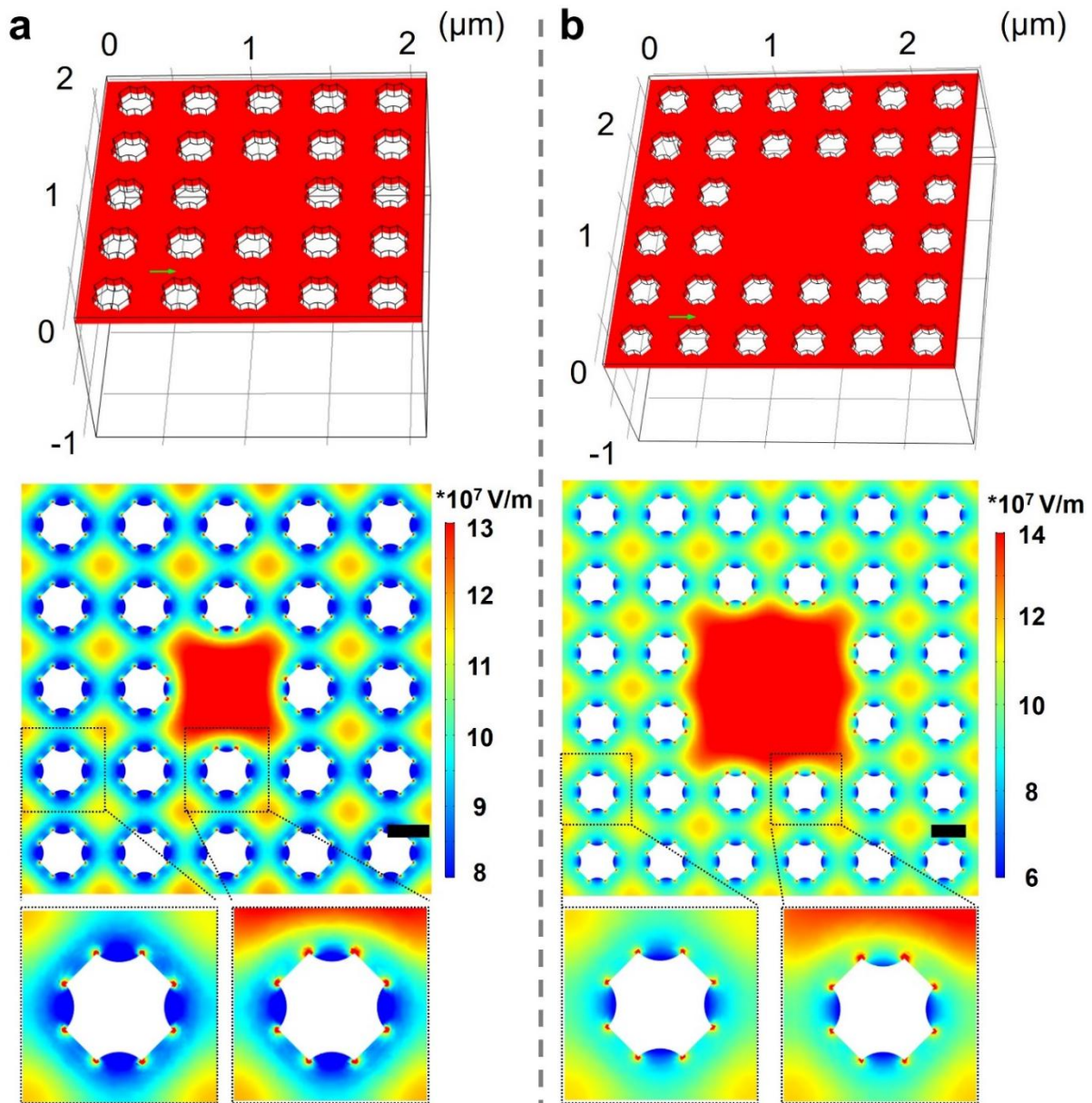


Supplementary Fig. 20 | Pore arrangement evolution of surface-patterned aluminium foils with mixture tetragonal and octagonal arrangements under different AVs. Schematic illustrations for (a) imprint stamp of tetragonal arrangement and (b) imprint stamp equipped with mixture tetragonal and octagonal arrangement. For obtaining the imprint stamp in (b), four neighboring nanopillars marked by pink color in (a) were removed using Zeiss FIB-SEMs system. (c) Surface-patterned aluminium foil using imprint stamp in (b). (d) Pore arrangement evolution of accessory octagonal arrangement under too low AVs, appropriate AVs, and too high AVs. The pores shown in (d) do not represent the real pore shapes. The gray cross, black cross, and hollow cross demonstrate the pore occurring at the site of predetermined nanodent, the emerging pore, and the disappearing pore from the site of predetermined nanodent, respectively. (e) Appropriate AV ranges for the basic L_T -spacing tetragonal arrangement, the accessory octagonal arrangement, and the mixture arrangement. $L_T = 400$ nm.

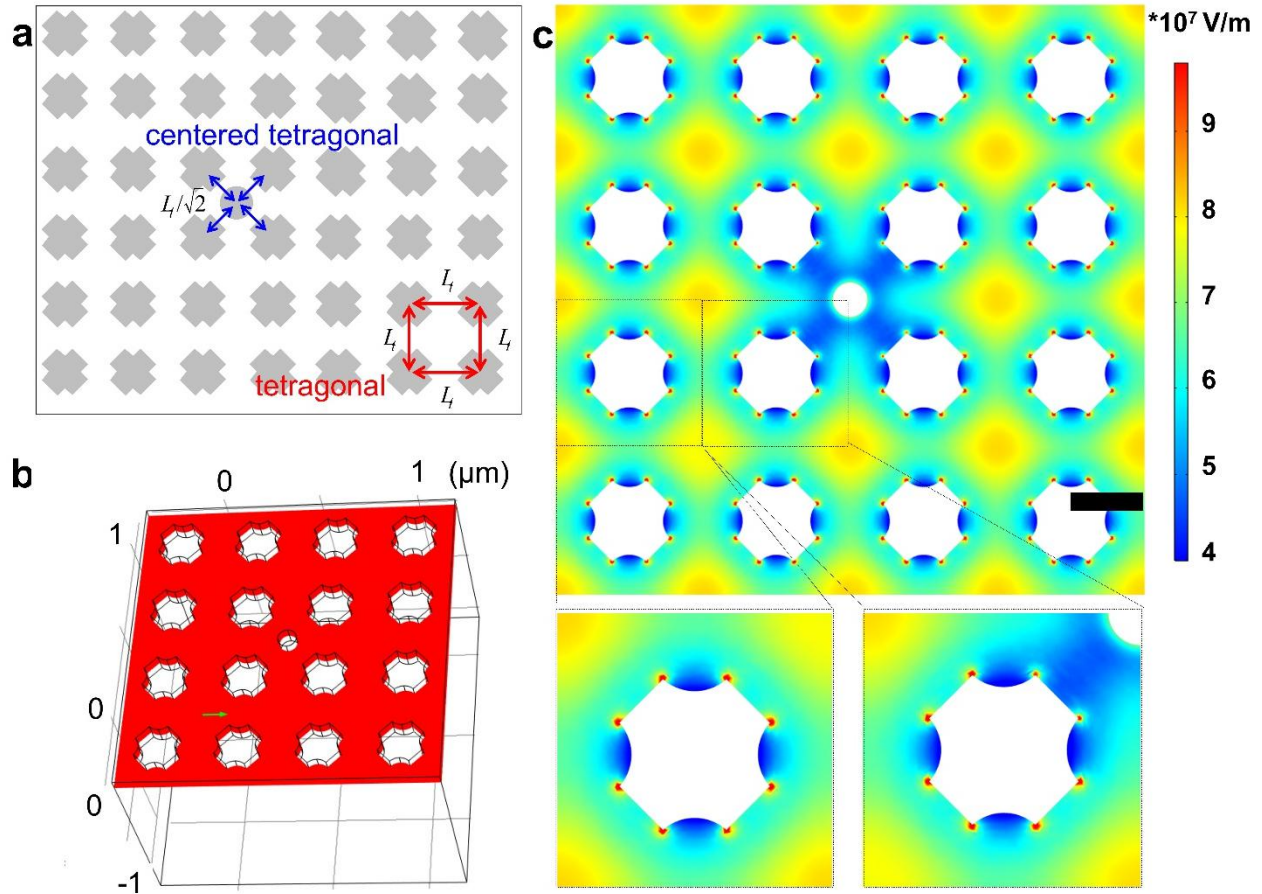
Following the same strategy introduced in Supplementary Fig. 18, to prevent the disappearance of diagonally neighboring pores during anodization for the octagonal arrangement (middle part of Supplementary Fig. 20d), the appropriate AVs should be lower than $\sqrt{5} V_b$ (that is, the high AV threshold defined by $0.4 \text{ V/nm} \times \sqrt{5} L_T$), where V_b corresponds to the conventional AV for the

basic L_t -spacing tetragonal arrangement and is defined by $0.4 \text{ V/nm} \times L_t$. And $\sqrt{5}L_t$ indicates the spacing of emerging arrangement (depicted by pink arrows) after the disappearance of diagonally neighboring pores from the octagonal arrangement under too high AVs, as shown in the right part of Supplementary Fig. 20d. Furthermore, to prevent the occurrence of a new pore at the central site of an octagonal unit during anodization, the appropriate AVs for the octagonal arrangement should be higher than $\sqrt{2.5} V_b$, that is, the low AV threshold defined by $0.4 \text{ V/nm} \times \sqrt{2.5}L_t$ where $\sqrt{2.5}L_t$ indicates the distance between the emerging pore at the central site of an octagonal unit and an existing pore (depicted by green arrows) under too low AVs, as shown in the left part of Supplementary Fig. 20d.

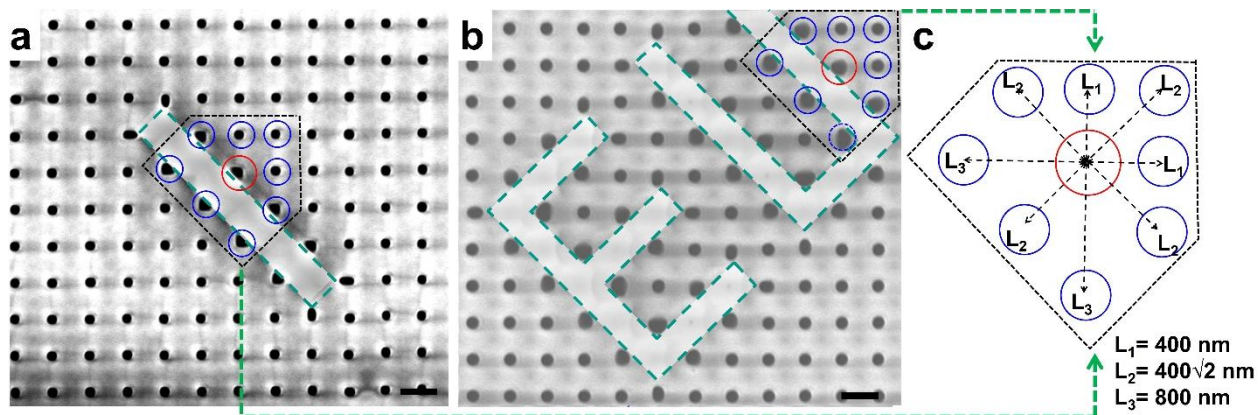
In theory, the appropriate AV ranges for two arrangements should be $(V_b\sqrt{2}, \sqrt{2} V_b)$ and $(\sqrt{2.5} V_b, \sqrt{5} V_b)$, respectively. Thus, there is no intersectional AV range for the tetragonal arrangement and the octagonal arrangement.

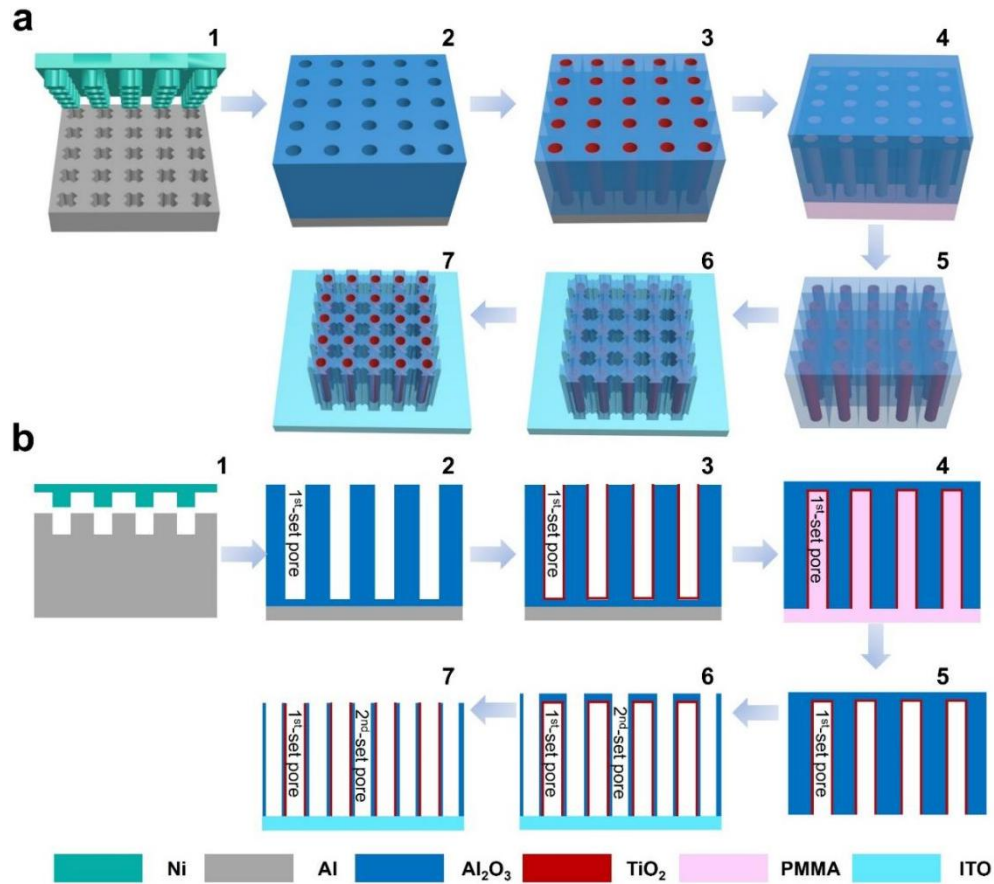


Supplementary Fig. 21 | COMSOL-simulated electric field maps across the near-surface lateral cross sections of surface-patterned aluminium foils. (a) Three-dimensional layout and electric field distribution for the surface-patterned aluminium foil with spacing-different tetragonal arrangements. The nanodent array is based on the configuration in Supplementary Fig. 18c. **(b)** Three-dimensional layout and electric field distribution for the surface-patterned aluminium foil with a mixture of tetragonal and octagonal arrangements. The nanodent array is based on the configuration in Supplementary Fig. 20c. For a clear comparison, the electric field maps in the basic (left, down) and accessory (right, down) arrangements are illustrated with higher magnification. Obviously, the electric field distribution in the accessory arrangement has higher asymmetry than that in the basic arrangement. All scale bars: 200 nm.



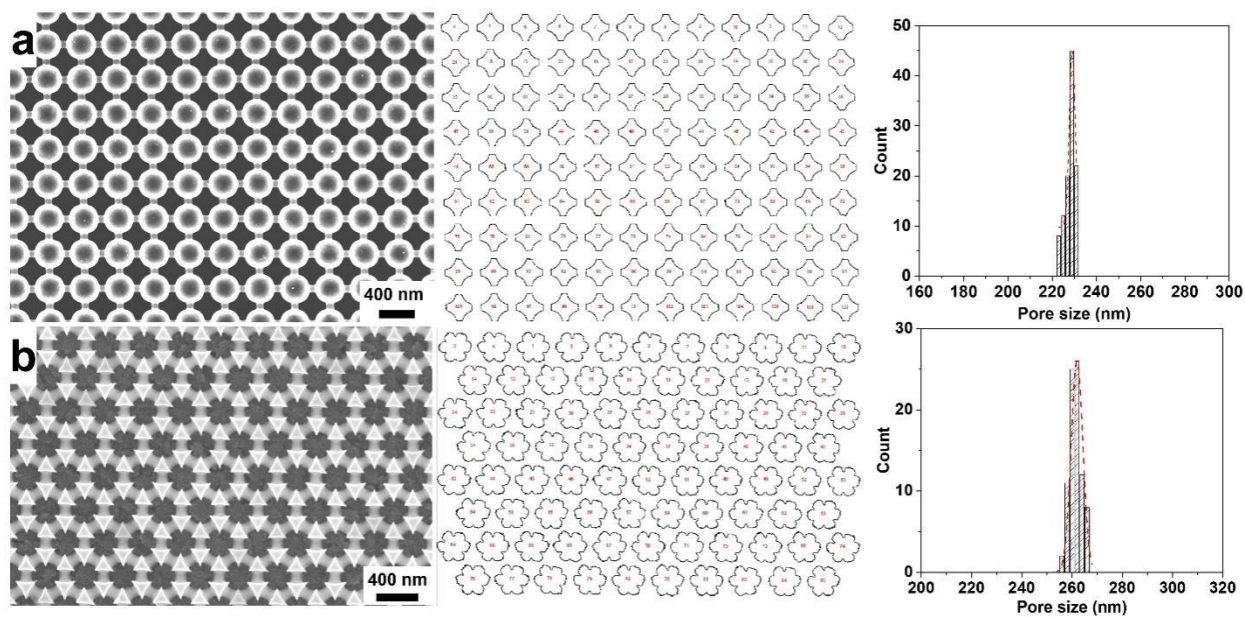
Supplementary Fig. 22 | COMSOL simulation for electric field map of surface-patterned aluminium foil with nanodents of the tetragonal and centered tetragonal arrangements. (a) Schematic illustration and **(b)** three-dimensional layout of surface-patterned aluminium foil in COMSOL simulation. For obtaining nanodents of mixture arrangement, we used a tetragonal imprint stamp to equip the aluminium surface with a tetragonal array of nanodents, followed by etching one more nanodent at the fourfold junction site of existing nanodents with Zeiss FIB-SEMs system. **(c)** COMSOL-simulated electric field maps across the near-surface lateral cross section. Scale bar: 200 nm.



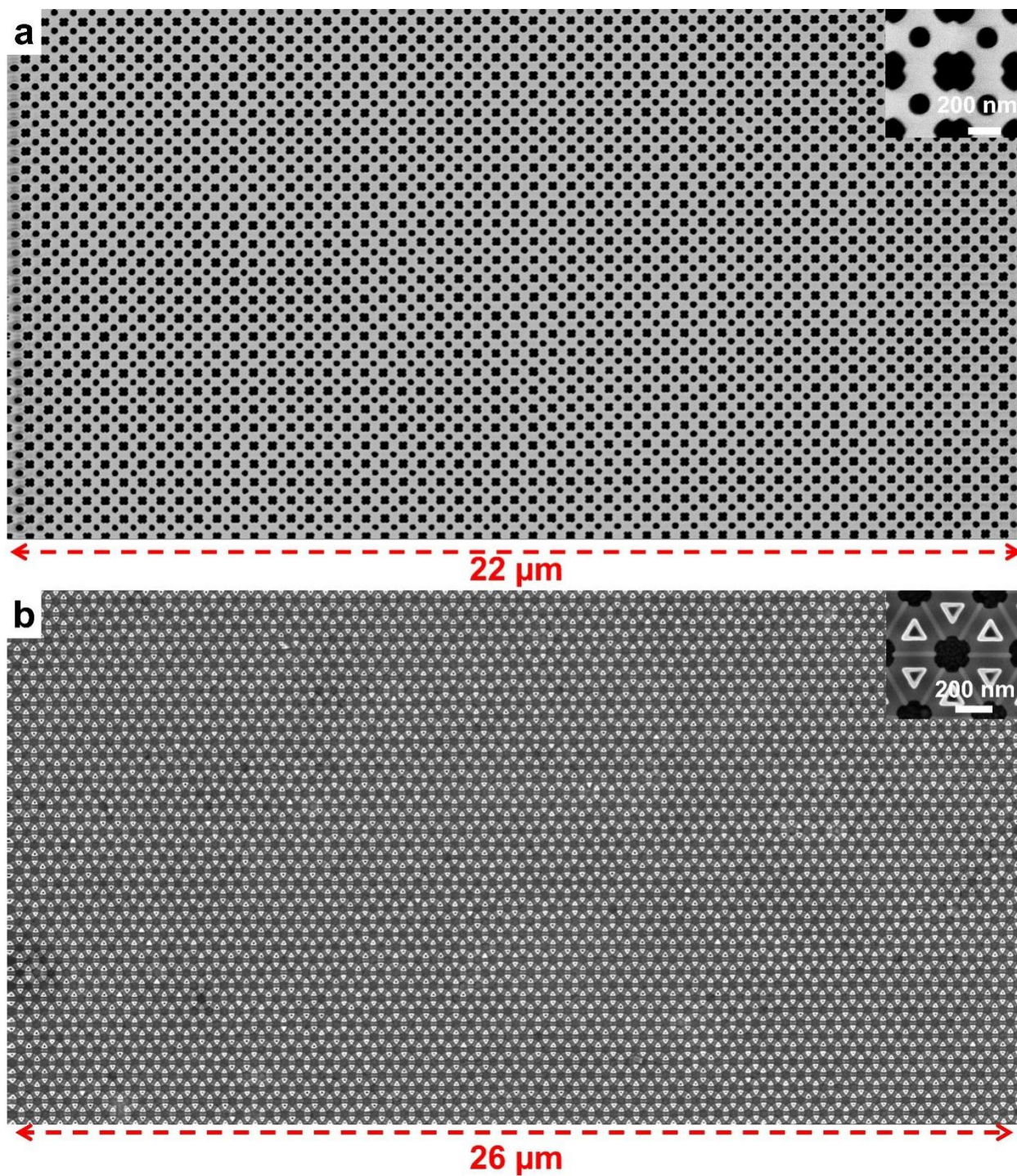


Supplementary Fig. 24 | Realization of the 2nd-set and two-set pores in AAO template.

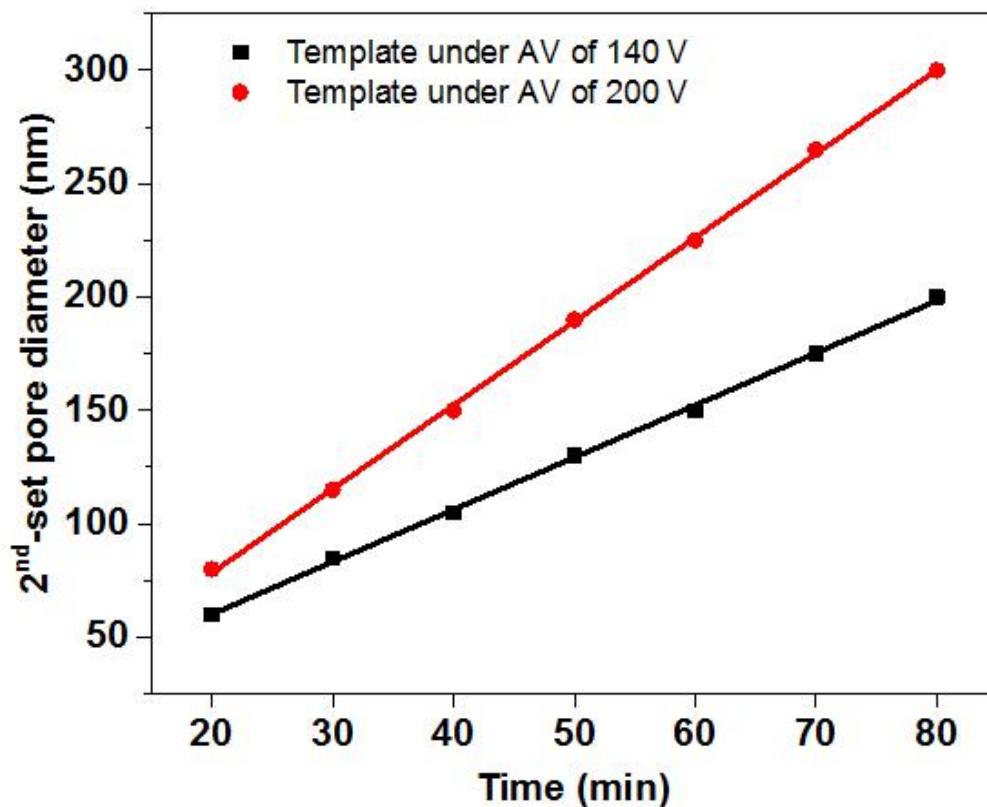
Schematic illustration of the fabrication process in (a) three-dimensional view and (b) two-dimensional cross-sectional view. The fabrication process includes seven procedures: (1) imprinting an aluminium foil; (2) anodizing the imprinted area to obtain the 1st-set pores; (3) coating a TiO₂ layer along the walls of the 1st-set pores to protect the 1st-set pores in the following etching procedures; (4) dripping PMMA over the as-anodized area to serve as a supporting scaffold to prevent the AAO template from cracking, followed by removing the unanodized aluminium; (5) dissolving PMMA by acetone; (6) opening the 2nd-set circular pores by using 0.1 M NaOH solutions, followed by reshaping the 2nd-set pores from a circular shape to a 4-edged cross shape because of uneven etching rates of pore walls in H₃PO₄ solutions, and then transferring the AAO template on an ITO substrate; (7) opening the 1st-set pores by ion-milling. Here the schematic illustration takes a tetragonal pore-arrangement template as an example, and the fabrication processes for templates with other pore arrangements (e.g., the hexagonal and mixture arrangements) are similar. The templates in Fig. 4b₁-b₄ and Fig. 4d₁-d₄ correspond to the 2nd-set pore arrays without removing the barrier layer of the 1st-set pores (procedure 6). And the templates in Figs. 4a₁,b₁ and 4c₁,d₁ correspond to the two-set pore arrays after ion-milling off the barrier layer of the 1st-set pores (procedure 7). Note that, the size and shape of the 2nd-set pores can be readily tuned by controlling etching time in NaOH and H₃PO₄ solutions, as evidenced by Fig. 4.



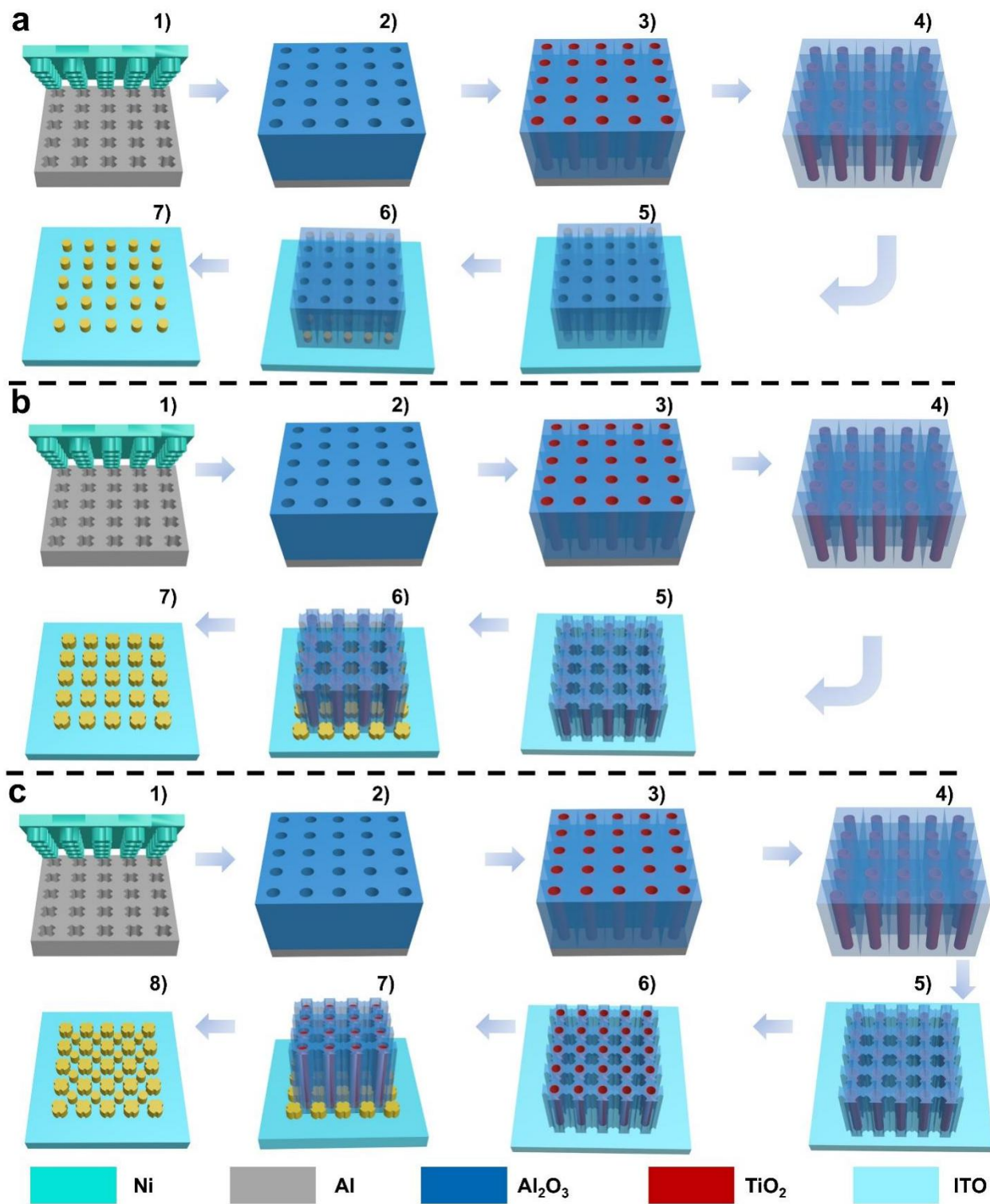
Supplementary Fig. 25 | Size distribution of the 2nd-set pores in AAO templates. The 2nd-set pores are arrayed in the (a) tetragonal and (b) trigonal arrangements.



Supplementary Fig. 26 | Large-area SEM images of AAO templates with two sets of shape-different pores: (a) the same type of template as the one in Fig. 4a₁b₃; (b) the same type of template as the one in Fig. 4c₁d₃. Insets: the corresponding SEM images with higher magnification.



Supplementary Fig. 27 | Dependence of the 2nd-set pore diameter on etching time in NaOH solutions. The templates were anodized under AVs of 140 V (black squares) and 200 V (red circles), respectively. According to the linear fitting analysis, the corresponding etching rates of the 2nd-set pores for two templates are about 2.3 and 3.7 nm/min, respectively.



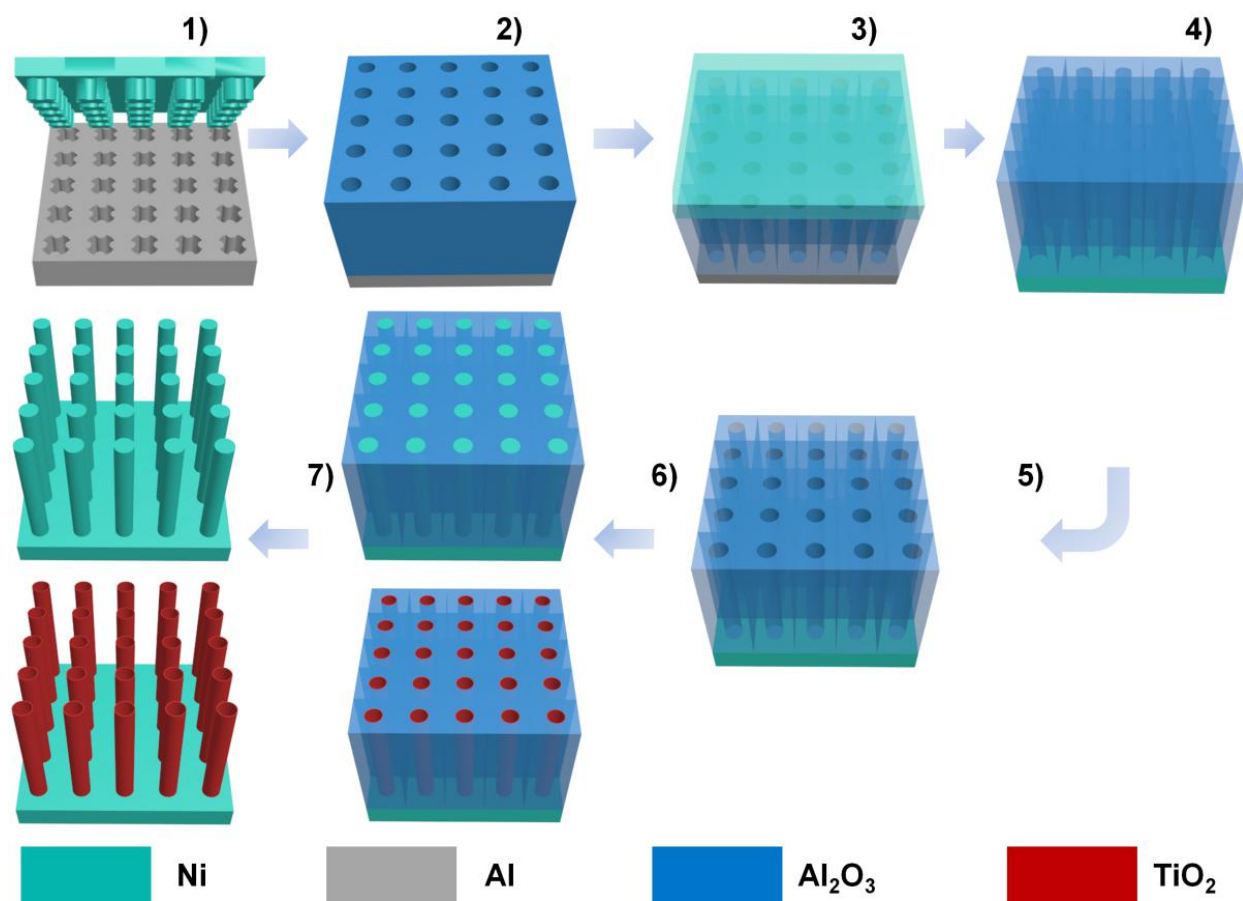
Supplementary Fig. 28 | Fabrication of zero-dimensional nanoparticle arrays using AAO template. Schematic illustration of the fabrication process of Au nanoparticles replicating the shapes of the (a) 1st-set, (b) 2nd-set, and (c) two-set pores, respectively.

To construct tetragonally arranged Au nanoparticles, the lab-made Ni imprint stamp with a tetragonal array of four-leaf clover-like nanopillars anchored on its surface was exploited for obtaining four-leaf clover-like nanodents on aluminium foil surface at a constant pressure of 10 kN cm^{-2} for 3min (Step 1). The imprinted area with periodic nanodents was anodized at an AV of 200 V, achieving a tetragonal array of circular pores (Step 2). After anodization, a 10-nm-thick TiO_2 layer was coated along the pore walls by ALD, followed by ion-milling off the TiO_2 layer at the top surface (Step 3). Then PMMA solution was dripped onto the anodized area of the aluminium foil and got dried naturally. With the dried PMMA as a supporting scaffold, the unanodized aluminium material was wet-chemically etched, finally achieving a thin template with circular pores after dissolving PMMA by acetone (Step 4).

In Supplementary Fig. 28a, the AAO template was then transferred onto an ITO substrate, followed by ion-milling off the barrier layer at the bottom of the 1st-set pores (Step 5). After completely opening the 1st-pores, Au material was evaporated onto the AAO template by PVD (Step 6). After peeling off the AAO template, an array of Au nanoparticles was obtained, which inherited the circular shape of the 1st-set pores (Step 7), as illustrated in Fig. 5a₁.

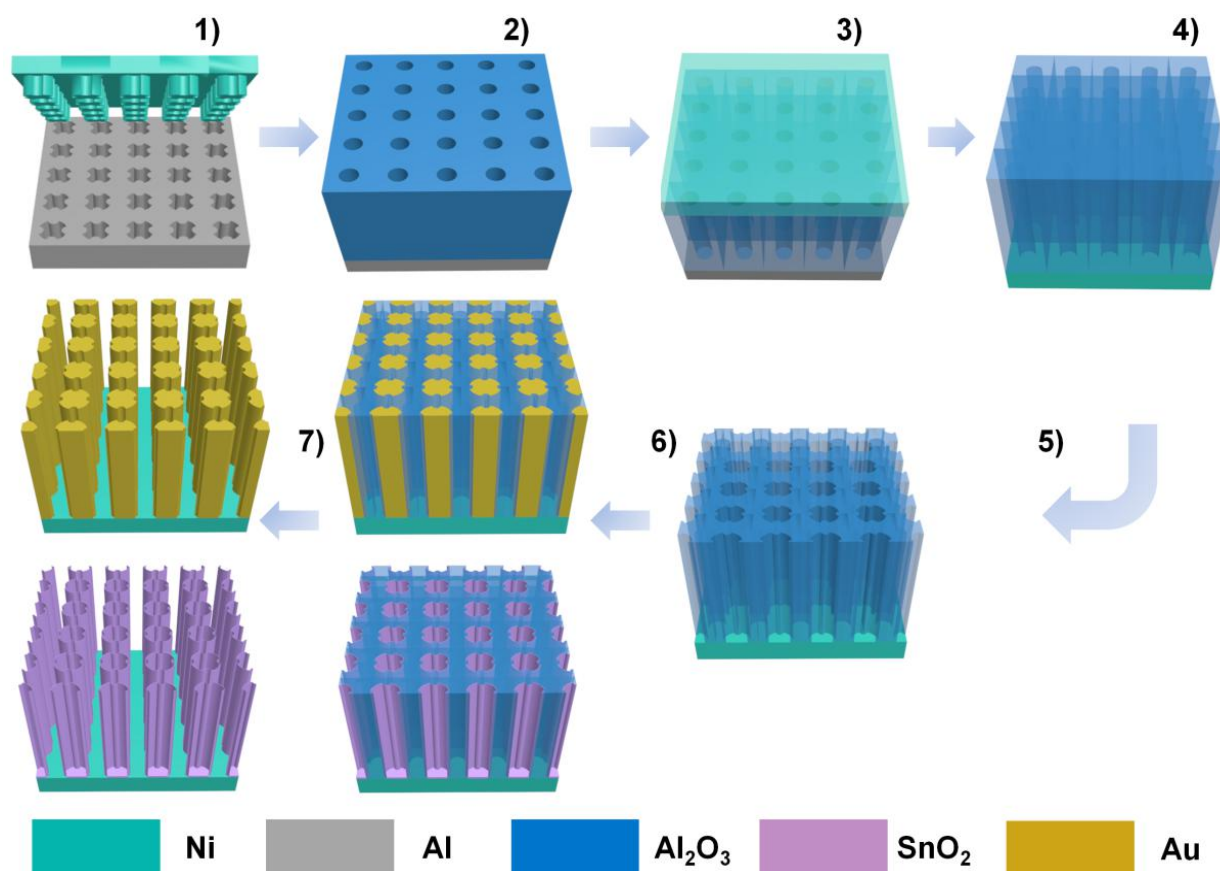
In Supplementary Fig. 28b, the AAO template was then immersed into 0.1 M NaOH solutions for 30 min, giving rise to the 2nd-set pores with a circular shape located at the junction sites of neighboring four 1st-set pores. The 2nd-set pores were further reshaped into a 4-edged cross shape in H_3PO_4 solutions. Afterwards, the AAO template owning the opened 2nd-set pores and the blocked 1st-set pores (without removing the barrier layer) was transferred onto an ITO substrate (Step 5). Finally, an array of Au nanoparticles replicating the 2nd-set pore shape was obtained after evaporating Au material (Step 6) and removing the template (Step 7), as illustrated in Fig. 5b₁.

In Supplementary Fig. 28c, after opening and reshaping the 2nd-set pores (Step 5), the barrier layer of the 1st-set pores was also ion-milled off, leading to an AAO template including two sets of completely opened pores (Step 6). In the same way, an array combining two sets of Au nanoparticles was obtained (Steps 7 and 8), as illustrated in Fig. 5c₁. The nanoparticle heights of all samples can be easily controlled by the PVD parameters such as evaporation rate and time.



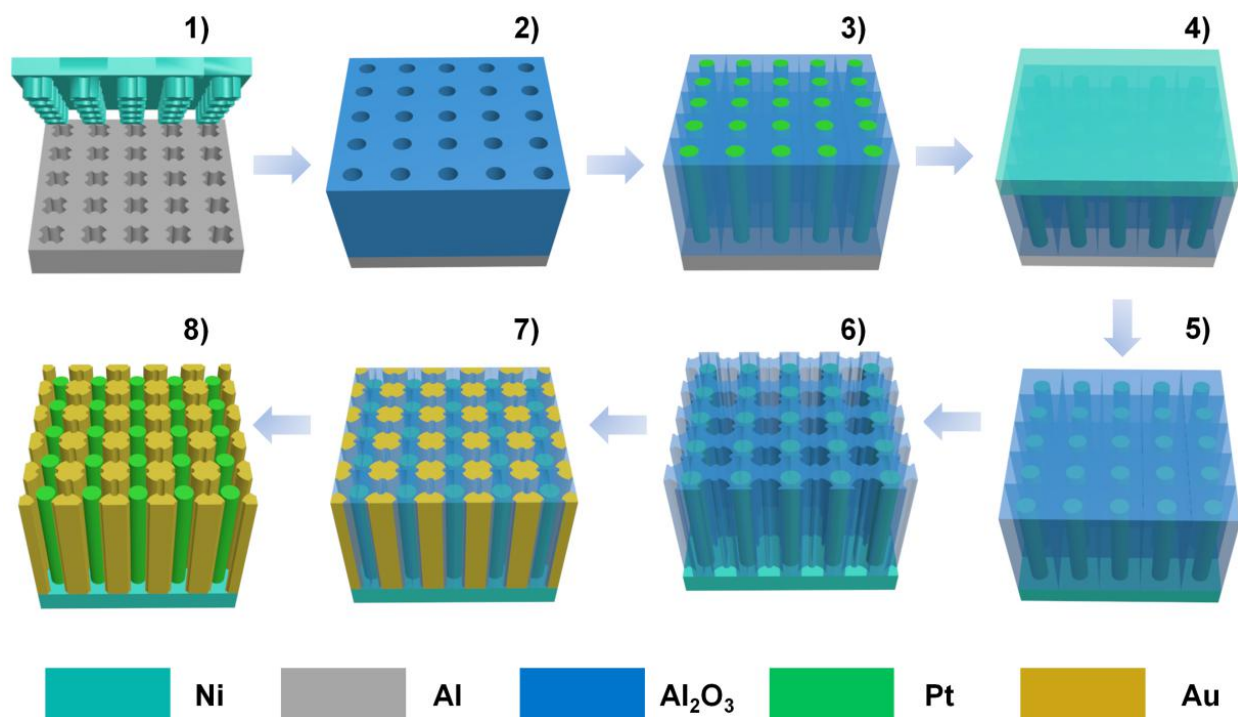
Supplementary Fig. 29 | Fabrication of one-dimensional nanostructure arrays using the 1st-set pores of AAO template.

After obtaining the 1st-set pores by anodizing surface-patterned aluminium foils according to the strategy introduced in Supplementary Fig. 28 (Steps 1 and 2), a conductive layer (5-nm-thick Ti and 20-nm-thick Au) was evaporated onto the top surface, followed by electrodeposition of a thick Ni layer (Step 3). Afterwards, the unanodized aluminium was wet-chemically etched (Step 4), and the exposed barrier layer of the 1st-set pores was ion-milled off (Step 5). Using the 1st-set pores as template, Ni nanowires were electrodeposited into the pores. Likewise, TiO₂ nanotubes can be produced along the pore walls by ALD, followed by ion-milling off the TiO₂ layer on the surface (Step 6). Finally, the AAO template was dissolved by NaOH solutions (Step 7), realizing arrays of Ni nanowires (Fig. 5a₂) and TiO₂ nanotubes (Fig. 5a₃) that replicated the circular shape of the 1st-set pores.



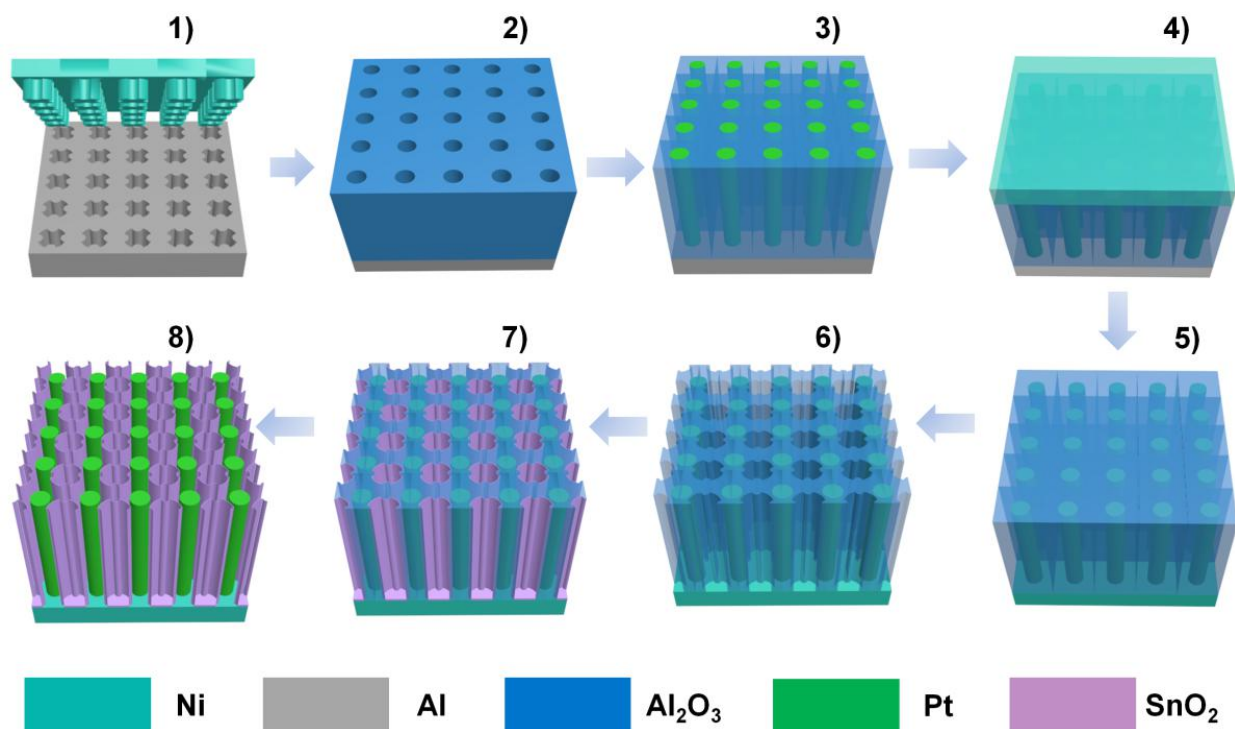
Supplementary Fig. 30 | Fabrication of one-dimensional nanostructure arrays using the 2nd-set pores of AAO template.

After anodizing surface-patterned aluminium foils following the approach introduced in Supplementary Fig. 28 (Steps 1 and 2), electrodepositing a thick Ni substrate with PVD-produced Ti/Au film as the working electrode (Step 3), and removing the unanodized aluminium (Step 4) according to the strategy used in Supplementary Fig. 29, the 2nd-set pores were opened in NaOH solutions and then reshaped in H₃PO₄ solutions (Step 5). After that, Au nanowires (or SnO₂ nanotubes) were grown into the 2nd-set pores by electrodeposition (or ALD), respectively (Step 6). After etching the AAO template in NaOH solutions, Au nanowires (or SnO₂ nanotubes) were constructed on the Ni substrate (Step 7), which were characterized by the 4-edged cross shape of the 2nd-set pores (Fig. 5b₂,b₃).



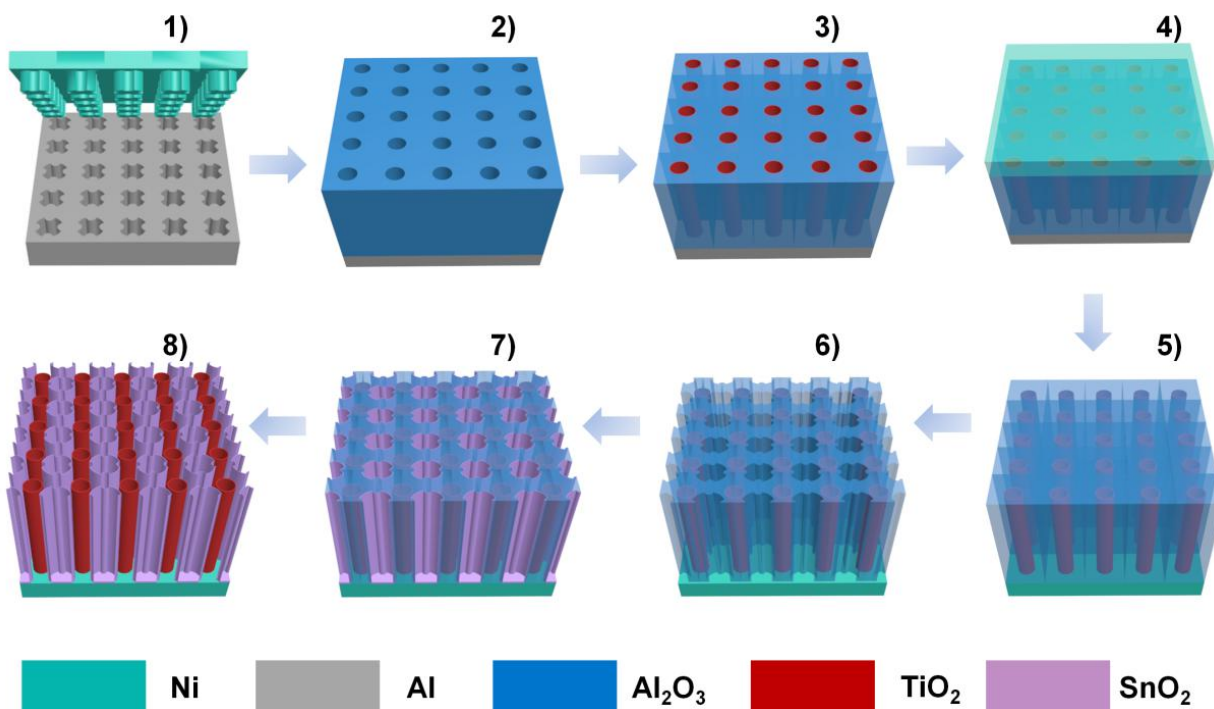
Supplementary Fig. 31 | Fabrication of nanowires/nanowires array using AAO template with pore combination.

After obtaining the 1st-set pores (Steps 1 and 2) according to the strategy stated in Supplementary Fig. 28, ALD of Pt material was performed to form Pt nanowires in the 1st-set pores (Step 3). Then, a thick Ni substrate was electrodeposited to support the AAO template (Step 4). The unanodized aluminium on the backside was then wet-chemically removed (Step 5). Upon the exposed AAO template, the 2nd-set pores were opened in NaOH solutions and then reshaped in H₃PO₄ solutions (Step 6). After exposing the conductive Ni substrate, electrodeposition was conducted to form Au nanowires in the 2nd-set pores (Step 7). Finally, the AAO template was wet-chemically etched, leading to a Pt-nanowires/Au-nanowires array on the Ni substrate (Step 8). As shown in Fig. 5c₂, the fabricated Pt-nanowires/Au-nanowires replicated the shapes of two sets of pores, respectively.



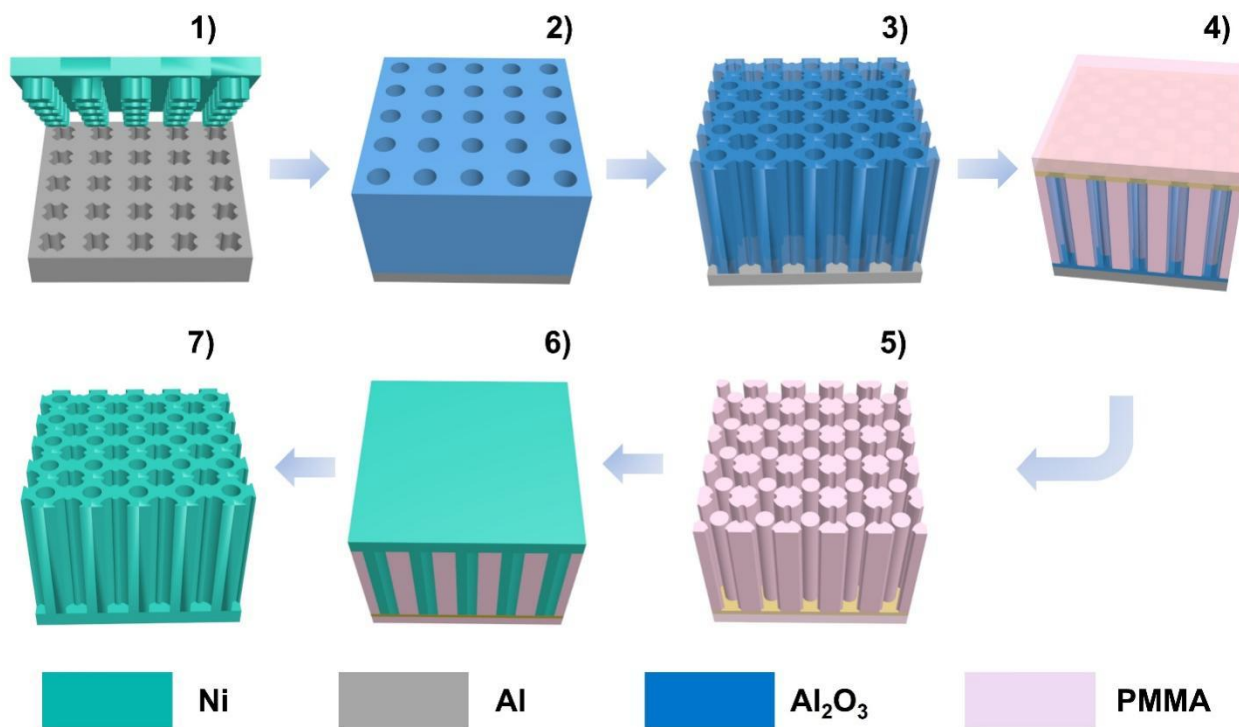
Supplementary Fig. 32 | Fabrication of nanowires/nanotubes array using AAO template with pore combination.

As for the Pt-nanowires/SnO₂-nanotubes array, Pt nanowires were formed in the 1st-set pores, and a thick Ni layer was then electrodeposited to support the AAO template, following the methods for the fabrication of Pt-nanowires/Au-nanowires array in Supplementary Fig. 31 (Steps 1 to 4). After wet-chemically removing the unanodized aluminium on the backside and etching the 2nd-set pores sequentially in NaOH solutions and H₃PO₄ solutions (Steps 5 and 6), a 20-nm-thick SnO₂ layer was coated along the 2nd-set pores by ALD, followed by ion-milling off the SnO₂ layer on the surface (Step 7). Finally, a Pt-nanowires/SnO₂-nanotubes array was constructed on the Ni substrate after removing the AAO template in NaOH solutions (Step 8). As shown in Fig. 5c₃, the fabricated Pt-nanowires/SnO₂-nanotubes replicated the shapes of two sets of pores, respectively.



Supplementary Fig. 33 | Fabrication of nanotubes/nanotubes array using AAO template with pore combination.

Regarding the fabrication of TiO₂-nanotubes/SnO₂-nanotubes arrays, the 1st-set pores were obtained following the strategy introduced in Supplementary Fig. 28 (Steps 1 and 2). Then, a 20-nm-thick TiO₂ layer was coated over the walls of the 1st-set pores, followed by ion-milling off the TiO₂ layer on the top surface (Step 3). Afterwards, a metallic layer (5-nm-thick Ti and 20-nm-thick Au) was evaporated onto the top surface of the aluminium foil by PVD. With this metallic layer as a conductive electrode, Ni electrodeposition was conducted to form a thick substrate (Step 4). The unanodized aluminium was removed, and the 2nd-set pores were then opened in the etching solutions (Steps 5 and 6). ALD was performed again to coat another SnO₂ layer along the walls of the 2nd-set pores, followed by ion-milling off the SnO₂ on the surface (Step 7). After wet-chemically dissolving the AAO template (Step 8), an array of TiO₂-nanotubes/SnO₂-nanotubes was constructed on the Ni substrate. As illustrated in Fig. 5c₄, the fabricated TiO₂-nanotubes/SnO₂-nanotubes replicated the shapes of two sets of pores, respectively.

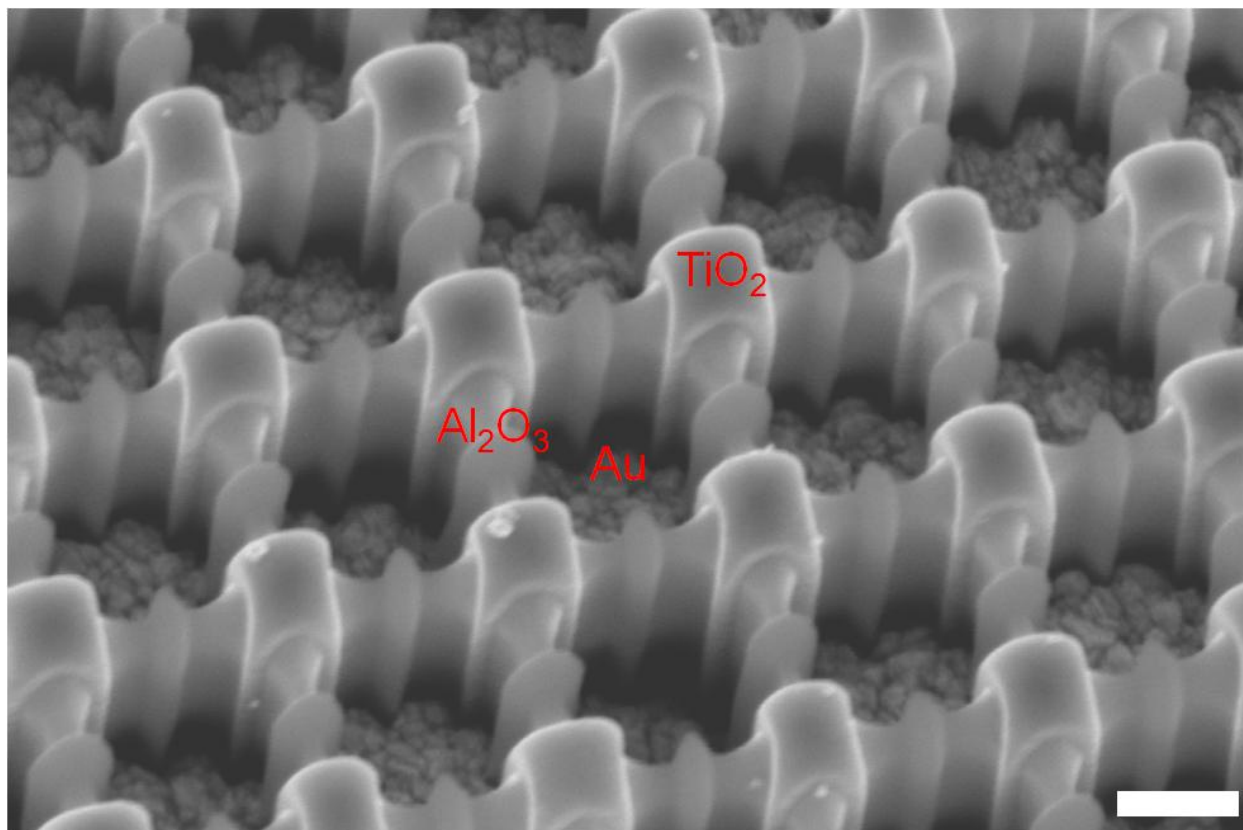


Supplementary Fig. 34 | Fabrication of Ni nanomesh using AAO template with pore combination.

After performing anodic anodization over surface-imprinted aluminium foils according to the approach introduced in Supplementary Fig. 28 (Steps 1 and 2), the barriers of the 2nd-set pores were thinned down by ion-milling, followed by pore-opening in NaOH solutions and then pore-resizing in H₃PO₄ solutions (Step 3). Upon the as-anodized area, a 20-nm-thick Au layer was evaporated by PVD at a low evaporation rate of 0.01 nm/min, followed by coating PMMA solution (Step 4). After naturally drying PMMA, the unanodized aluminium and the AAO template were wet-chemically removed (Step 5). Afterwards, Ni deposition was performed with the exposed Au layer as working electrode (Step 6). Finally, PMMA was dissolved by acetone, leading to a Ni nanomesh with two sets of pores (Step 7), as illustrated in Fig. 5c₅.



Supplementary Fig. 35 | Large-area hexagonal array of Ag nanoparticles with internally-bent triangular shape. This SEM image is obtained from the sample S3 (shown in Fig. 6a), which is characterized by the best device performance. The Ag nanoparticles possess reliable structural uniformity, which is in favor of yielding homogeneous and reproducible SERS signals over large areas.



Supplementary Fig. 36 | TiO₂-nanotubes/Au-nanowires combination in AAO template. Scale bar: 200 nm.

References:

1. Johnson, P. B. & Christy, R.-W. Optical constants of the noble metals. *Phys. Rev. B* **6**, 4370-4379 (1972).
2. Siefke, T. *et al.* Materials pushing the application limits of wire grid polarizers further into the deep ultraviolet spectral range. *Adv. Opt. Mater.* **4**, 1780-1786 (2016).
3. Vrublevsky, I., Parkoun, V., Sokol, V., Schreckenbach, J. & Marx, G. The study of the volume expansion of aluminum during porous oxide formation at galvanostatic regime. *Appl. Surf. Sci.* **222**, 215-225 (2004).
4. Lee, W. & Park, S.-J. Porous anodic aluminum oxide: anodization and templated synthesis of functional nanostructures. *Chem. Rev.* **114**, 7487-7556 (2014).
5. Nielsch, K., Choi, J., Schwirn, K., Wehrspohn, R. B. & Gösele, U. Self-ordering regimes of porous alumina: the 10 porosity rule. *Nano Lett.* **2**, 677-680 (2002).